

The properties of dwarf spheroidal galaxies in the Cen A group

Stellar populations, internal dynamics, and a heart-shaped H α ring^{*,**}

Oliver Müller¹, Katja Fahrion², Marina Rejkuba², Michael Hilker², Federico Lelli³, Katharina Lutz¹,
Marcel S. Pawłowski⁴, Lodovico Coccato², Gagandeep S. Anand⁵, and Helmut Jerjen⁶

¹ Observatoire Astronomique de Strasbourg (ObAS), Université de Strasbourg – CNRS, UMR 7550, Strasbourg, France
e-mail: oliver.muller@astro.unistra.fr

² European Southern Observatory, Karl-Schwarzschild Strasse 2, 85748 Garching, Germany

³ School of Physics and Astronomy, Cardiff University, Queens Buildings, The Parade, Cardiff CF24 3AA, UK

⁴ Leibniz-Institut für Astrophysik Potsdam (AIP), An der Sternwarte 16, 14482 Potsdam, Germany

⁵ Institute for Astronomy, University of Hawaii, 2680 Woodlawn Drive, Honolulu, HI 96822, USA

⁶ Research School of Astronomy and Astrophysics, Australian National University, Canberra, ACT 2611, Australia

Received 7 September 2020 / Accepted 4 October 2020

ABSTRACT

Dwarf spheroidal galaxies (dSphs) have been extensively investigated in the Local Group, but their low luminosity and surface brightness make similar work in more distant galaxy groups challenging. Modern instrumentation unlocks the possibility of scrutinizing these faint systems in other environments, expanding the parameter space of group properties. We use MUSE spectroscopy to study the properties of 14 known or suspected dSph satellites of Cen A. Twelve targets are confirmed to be group members based on their radial velocities. Two targets are background galaxies at ~ 50 Mpc: KK 198 is a face-on spiral galaxy, and dw1315–45 is an ultra-diffuse galaxy with an effective radius of ~ 2300 pc. The 12 confirmed dSph members of the Cen A group have old and metal-poor stellar populations and follow the stellar metallicity–luminosity relation defined by the dwarf galaxies in the Local Group. In the three brightest dwarf galaxies (KK 197, KKs 55, and KKs 58), we identify globular clusters, as well as a planetary nebula in KK 197, although its association with this galaxy and/or the extended halo of Cen A is uncertain. Using four discrete tracers, we measure the velocity dispersion and dynamical mass of KK 197. This dSph appears dark matter dominated and lies on the radial acceleration relation of star-forming galaxies within the uncertainties. It also is consistent with predictions stemming from modified Newtonian dynamics. Surprisingly, in the dwarf KK 203 we find an extended H α ring. Careful examination of *Hubble* Space Telescope photometry reveals a very low level of star formation at ages between 30 and 300 Myr. The H α emission is most likely linked to a ~ 40 Myr old supernova remnant, although other possibilities for its origin cannot be entirely ruled out.

Key words. galaxies: dwarf – galaxies: kinematics and dynamics – galaxies: stellar content – Galaxy: abundances

1. Introduction

Dwarf galaxies make up the bulk of galaxies in the Universe (Binggeli et al. 1990; Ferguson & Binggeli 1994). Typically, they are defined as galaxies less luminous than -17 mag in the V-band (Tammann 1994; Tolstoy et al. 2009), as galaxies with stellar masses below a few times $10^9 M_{\odot}$ (Bullock & Boylan-Kolchin 2017; McGaugh et al. 2017), or as galaxies with circular velocities below 100 km s^{-1} (Lelli et al. 2014). These constraints roughly coincide with the properties of the Small Magellanic Cloud (SMC) and set dwarf galaxies apart from giant galaxies. Dwarf galaxies are separated into gas-rich dwarfs with ongoing star formation – including dwarf irregulars (dIrrs) and blue compact dwarfs (BCDs) – and gas-poor dwarfs with predominantly old stellar populations. The former ones are typically found in the field environment, in galaxy groups, and in the outer parts of

galaxy clusters, while the latter are almost exclusively found in galaxy clusters and as satellites of massive spirals and ellipticals (Binggeli et al. 1990; Geha et al. 2012).

For historical reasons, the taxonomy of gas-poor dwarfs is complex (Binggeli 1994) and includes three common nomenclatures: (i) Dwarf ellipticals (dEs) have been predominantly found in galaxy clusters (Sandage & Binggeli 1984) and make up the bright end of the dwarf galaxy population from $\sim 10^9$ down to $\sim 10^7 L_{\odot}$; (ii) dwarf spheroidals (dSphs) have traditionally been studied in the Local Group (Mateo 1998) and constitute an intermediate luminosity range from $\sim 10^7$ to $\sim 10^5 L_{\odot}$; and (iii) ultrafaint dwarfs (UFDs) were discovered in the Local Group after the advent of the Sloan Digital Sky Survey (SDSS, York et al. 2000) and other deep optical surveys and represent the faintest galaxies known, with luminosities from $\sim 10^5$ to $\sim 10^3 L_{\odot}$ (e.g., Willman et al. 2005; Belokurov et al. 2007; Koposov et al. 2015; Kim & Jerjen 2015; Mau et al. 2020). All these gas-poor dwarfs, however, form a single sequence in structural diagrams comparing stellar luminosity, effective radius, and effective surface brightness (Tolstoy et al. 2009; Kormendy et al. 2009). In fact, next-generation surveys of the Virgo and Fornax clusters have started to probe gas-poor dwarfs down to luminosities of $\sim 10^5 L_{\odot}$ (Ferrarese et al. 2016; Eigenthaler et al. 2018;

* The fully reduced data cubes are only available at the CDS via anonymous ftp to [cdsarc.u-strasbg.fr](ftp://cdsarc.u-strasbg.fr) (130.79.128.5) or via <http://cdsarc.u-strasbg.fr/viz-bin/cat/J/A+A/645/A92>

** Based on observations collected at the European Organisation for Astronomical Research in the Southern Hemisphere under ESO program 0101.A-0193(A) and 0101.A-0193(B).

Venhola et al. 2019), blurring the traditional difference between cluster dEs and Local Group dSphs.

The most detailed studies of dSphs have been carried out in the Local Group (e.g., Tolstoy et al. 2004, 2009; Koch et al. 2006; Battaglia et al. 2006, 2011; Martin et al. 2008; Tafelmeyer et al. 2010; Kirby et al. 2011; Hidalgo et al. 2013; Weisz et al. 2014; Taibi et al. 2018, 2020), where we can observe their stars down to faint main sequence evolutionary phases and measure individual stellar velocities and their chemical abundances, thereby constraining the formation and evolution of the hosts. Due to their low luminosities and low surface brightnesses, the physical characterization of dSphs beyond the Local Group is inherently difficult. However, as these low-mass systems hold some of the fundamental observational constraints for cosmology (Bullock & Boylan-Kolchin 2017), there is a growing effort to search for and study them in a range of environments, as enabled by modern, highly sensitive instruments (e.g., Jerjen & Rejkuba 2001; Rejkuba et al. 2006; Lisker et al. 2008; Da Costa et al. 2010; Lianou et al. 2010; Crnojević et al. 2010, 2011a; Weisz et al. 2011; Ryš et al. 2013; Makarov et al. 2015; Toloba et al. 2015; Stein et al. 2018; Danieli et al. 2019; Müller et al. 2019a; Chilingarian et al. 2019; Bennet et al. 2019; Hamraz et al. 2019; Venhola et al. 2019; Scott et al. 2020; Gannon et al. 2020).

Globular clusters (GCs) do exist in all major galaxies. In the regime of dwarf galaxies, however, the presence of GC systems around them becomes stochastic (e.g., Georgiev et al. 2010). In the Milky Way system, only four dwarf galaxies have a population of old and massive globular clusters. These are the SMC (Mackey & Gilmore 2003a), the tidally disrupting Sagittarius dwarf spheroidal (Mackey & Gilmore 2003b), Fornax (Mackey & Gilmore 2003b), and the ultra-faint dwarf Eridanus 2 (Crnojević et al. 2016a). The remaining dwarfs host no known GCs (Huang & Koposov 2021). Thus, a key question arises: Are the Milky Way dwarf galaxies a representative sample of the general population of dwarf galaxies (see e.g., Geha et al. 2017)? In galaxy clusters, a plethora of GCs have been found associated with dwarf galaxies (e.g., Strader et al. 2006; Prole et al. 2019; Forbes et al. 2020), with observed numbers of GCs larger than for the Milky Way dwarfs. This is explained by a higher GC formation efficiency in dwarf galaxies living in denser environments (Peng et al. 2008). However, for the intermediate range of galactic environments there is still a lack of data. Surveys like the Mass Assembly of early Type gaLaxies with their fine Structures (MATLAS, Duc et al. 2015) or the Dwarf Galaxy Survey with Amateur Telescopes (DGSAT, Javanmardi et al. 2016) aim to fill this gap by targeting massive elliptical and spiral galaxies in the nearby field ($10 < D < 45$ Mpc).

The closest giant elliptical galaxy to us – Centaurus A (Cen A) at a distance of 3.8 Mpc (Harris et al. 2010) – is the ideal environment for detailed studies of dwarf galaxies since it is possible to investigate their physical properties using both deep imaging observations that resolve individual bright stars (Karachentsev et al. 2002; Rejkuba et al. 2006; Crnojević et al. 2010, 2012, 2019; Müller et al. 2019b) and imaging of their integrated light properties (Crnojević et al. 2016b; Taylor et al. 2016, 2017, 2018; Müller et al. 2017). Regarding spectroscopic observations, the most recent integral-field observations of the two dSphs KKs58 and KK197 in the Cen A group revealed nuclear star clusters (NSCs) and GCs associated with them (Fahrion et al. 2020a). The simultaneous extraction of the metallicity of both the NSC and the galaxy stellar body showed that these NSCs are more metal-poor than their hosts, suggesting that they have formed through the process of in-spiraling GCs. Intriguingly, the masses, sizes, and metallicities of these two NSCs are

consistent with the properties of known ultra-compact dwarfs (Misgeld & Hilker 2011; Voggel et al. 2018, 2020; Fahrion et al. 2019a), suggesting that stripped nuclei of dwarf galaxies are the progenitors of low-mass ultra-compact dwarfs (Strader et al. 2013).

These two dwarf galaxies are part of a larger survey aiming to study the phase-space distribution of the dwarf galaxy satellites around Cen A (Tully et al. 2015; Müller et al. 2016, 2018a). The survey has two main components: (i) deep imaging to resolve individual bright red giant stars and measure distances to dwarf galaxies by means of the tip of the red giant branch (TRGB) method, and (ii) integrated light spectroscopy to measure the dwarfs' radial velocities. In the first part we used FORS2 at VLT to derive accurate distances, thereby also confirming group membership, and measure mean photometric metallicities and structural parameters for nine dwarf satellites of Cen A (Müller et al. 2019b). In this article, we present the MUSE spectroscopic data analysis of 14 putative dwarf galaxies in our survey, study their individual properties, and compare them to Local Group dwarf galaxies. In a companion paper, we will explore the dynamical properties of the whole satellite system.

2. Observations and data reduction

The data were acquired with the MUSE integral field spectrograph mounted at UT4 of the VLT on Cerro Paranal, Chile (Bacon et al. 2010) as part of a 46 h program (PI: Müller, proposal ID: 0101.A-0193) designed to measure distances (requiring 26 h with FORS2) and line-of-sight velocities (20 h with MUSE) of dwarf galaxy candidates. The targets were selected from Müller et al. (2017) and Karachentsev et al. (2004, 2013) as the most likely members of the Cen A group that could be detected by MUSE with reasonable integration times. We used the Wide Field Mode (WFM) of MUSE, providing a field-of-view (FOV) of $1' \times 1'$ sampled at $0''.2 \text{ pix}^{-1}$. The observed galaxies have sizes of $\sim 1'$, which fit well in the MUSE FOV. The instrument was used in its nominal wavelength setting covering 480–930 nm with a mean resolution of 3000^1 . Given that our primary goal was to obtain the systemic velocity by binning the signal from the entire target galaxy, it was possible to conduct the observations under relatively poor seeing conditions and sometimes with thin clouds, meaning filler conditions, in service mode between April and June 2018.

Depending on the galaxy's mean surface brightness we required one or two Observation Blocks (OBs). For eight targets with higher surface brightness, the single OB included four science exposures (O), each 500 s long, interleaved with two offset sky exposures (S) of 250 s. Hence, the OB had the following sequence of exposures: OSO OSO. The other six targets with lower surface brightness had two OBs per target, each with an OSO strategy. In this case, the science and offset exposures had 1160 s and 580 s, respectively. We employed our FORS2 images – where possible – to select empty regions for the offset sky exposures, otherwise we used DECam or DSS images.

The MUSE Internal Data Products are available from the ESO Science Archive, which includes products run through the MUSE pipeline version 2.2 (Weilbacher et al. 2012, 2020). The data have been preprocessed, bias and flat-field corrected, astrometrically calibrated, sky-subtracted, wavelength and flux

¹ The resolving power ranges between 1770 at 480 nm and 3590 at 930 nm in the WFM.

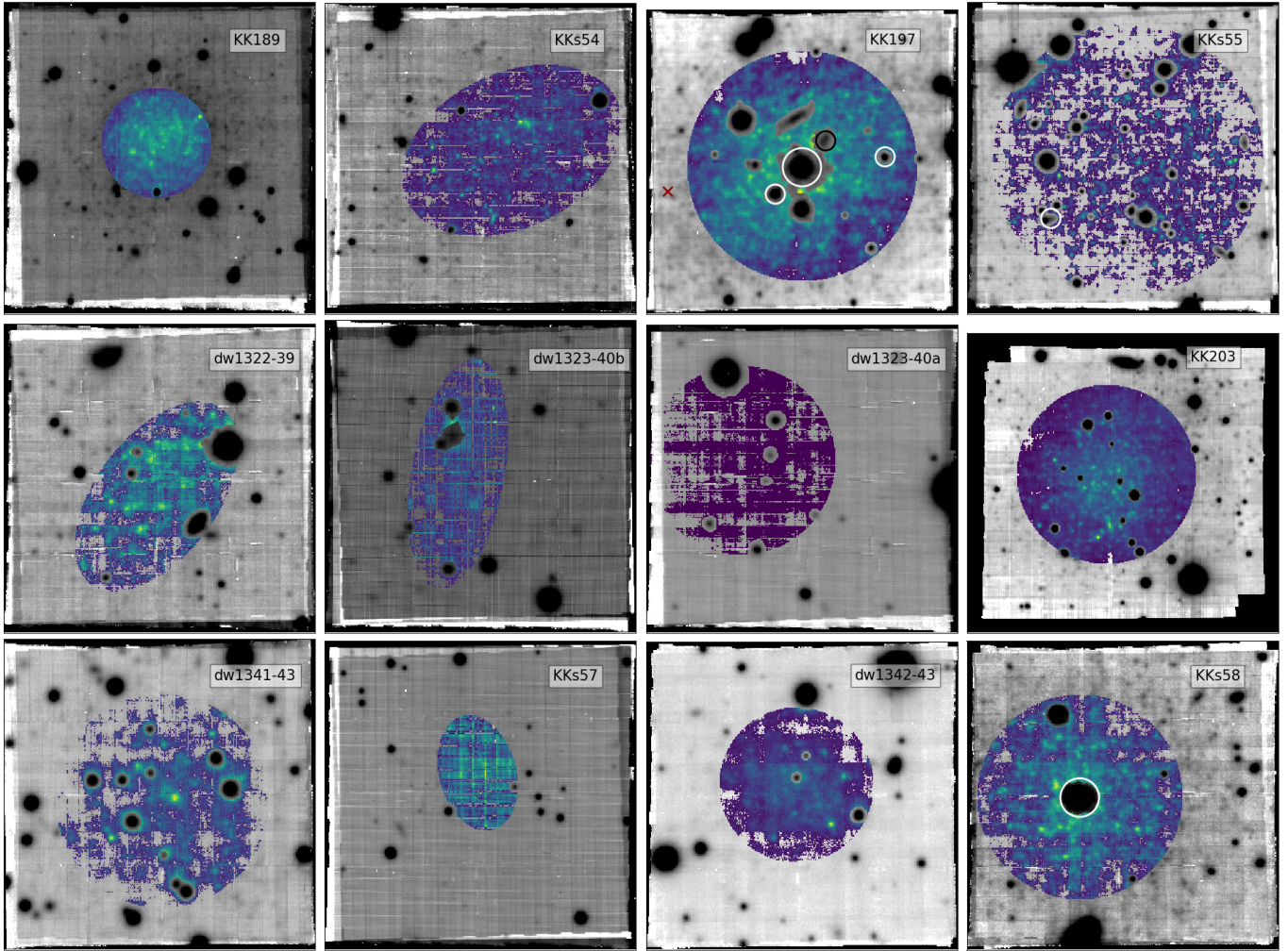


Fig. 1. Collapsed, white-light images of the dwarf galaxies confirmed to be Cen A group members. The regions where we extracted the spectra are indicated in color. The NSC are indicated with the large white circles, the GCs as small white circles, the stellar association as small black circle, and the position of the PN is marked with a red cross. The images show the entire MUSE FOV – 1' per side – which corresponds to 1.1 kpc at a mean distance of the Cen A group (3.8 Mpc), and are oriented with north up and east to the left.

calibrated (Hanuschik et al. 2017)². The sky subtraction makes use of the offset sky exposures. To further reduce the sky residual lines, we applied the Zurich Atmosphere Purge (ZAP) principal component analysis algorithm (Soto et al. 2016). We tested whether the offset sky exposure or empty patches on the science exposure lead to better results in removing sky residuals. For objects having at least 20% of sky in the science exposure, we got better results with these empty patches than using the offset sky exposure, therefore we used the former where applicable. To select the empty sky patches on the science exposures we ran the MTOObjects tool (Teeninga et al. 2013, 2015), which creates a segmented fits file with all detected sources. This segmentation map served as input mask for ZAP. In some cases, we also manually masked the outskirts of the target galaxies or undetected objects to further improve the quality of the sky subtraction.

We extracted the integrated spectra using an elliptical aperture, which was derived from the optical images of the galaxies. Foreground stars and background objects were masked using the python implementation *sep* (Barbary 2016) of Source Extractor

(Bertin & Arnouts 1996). Furthermore, we masked pixels with negative mean flux as a simple constrain on the signal-to-noise ratio (S/N) per spaxel. The size of the aperture was chosen to optimize the S/N. Figure 1 shows the white light images with highlighted target extraction areas.

2.1. Radial velocity and stellar population measurements

To extract line-of-sight velocities and stellar population properties from the galaxy spectra, we employed pPXF (Cappellari & Emsellem 2004), a standard routine in fitting line-of-sight velocity distributions from absorption-line spectra. We followed the same methodology as described in several previous studies (Emsellem et al. 2019; Fensch et al. 2019; Müller et al. 2020). In short, we use a set of Single Stellar Population (SSP) spectra from the eMILES library (Vazdekis et al. 2016), with metallicities [M/H] ranging from solar down to -2.27 dex and ages from 70 Myr to 14.0 Gyr. We assume a Kroupa initial mass function (IMF, Kroupa 2001). The spectra from the SSP library are convolved with the line-spread function as described in Guérou et al. (2017, see also Appendix of Emsellem et al. 2019). A variance spectrum was measured on the masked data cube and added to pPXF to improve the fitting. For the kinematic fit, we

² See also <http://www.eso.org/observing/dfo/quality/PHOENIX/MUSE/processing.html>

Table 1. Observation summary for the 14 dwarf galaxy candidates.

Name	α_{2000} (hh:mm:ss.s) (1)	δ_{2000} (dd:mm:ss) (2)	Observing date (3)	Nexp (4)	Exptime (s) (5)	AM (6)	IQ (") (7)	S/N (8)	Note (9)
KK189	13:12:45.1	-41:49:55	7/8 May 2018	4	500	1.07	0.7	28.5	Thin clouds
KKs54	13:21:32.3	-31:53:10	7/8 May 2018	4	500	1.09	0.7	12.1	Thin clouds
KK197	13:22:01.9	-42:32:07	15/16 Apr 2018	2	1160	1.20	1.2	27.6	Clear sky
KKs55	13:22:12.4	-42:43:50	8/9 May 2018	3	1160	1.05	1.2		Extra exposure due to thin/thick clouds
			19/20 May 2018	2	1160	1.05	0.8	14.4	Clear/thin
			20/21 May 2018	2	1160	1.09	0.7		Thin clouds
dw1322-39	13:22:32.0	-39:54:19	8/9 May 2018	4	500	1.17	1.5	11.9	Thin clouds
dw1323-40b	13:23:55.0	-40:50:08	5/6 Jun 2018	4	1160	1.11	1.3	13.1	Thin/clear
dw1323-40a	13:24:53.0	-40:45:40	8/9 May 2018	4	500	1.35	1.7	9.3	Thin clouds
KK203	13:27:27.6	-45:21:08	19/20 May 2018	5	1160	1.28	0.6	24.0	Extra exposure due to a technical issue
dw1341-43	13:41:36.9	-43:51:16	5/6 Jun 2018	4	1160	1.06	1.3	12.9	Mostly clear sky
KKs57	13:41:37.9	-42:34:54	7/8 May 2018	4	500	1.20	0.8	13.3	Thin clouds
dw1342-43	13:42:43.9	-43:15:18	11/12 May 2018	4	500	1.16	1.4	17.8	Clear sky
KKs58	13:46:00.1	-36:19:43	8/9 May 2018	4	500	1.04	1.5	17.7	Thin clouds
KK198	13:22:56.0	-33:34:21	9/10 Jun 2018	4	500	1.09	0.8	-	Not Cen A group member; thin clouds
dw1315-45	13:15:56.0	-45:45:02	7/8 May 2018	4	1160	1.28	0.6	-	Not Cen A group member; thin clouds

Notes. (1) and (2): Coordinates of the center of observation (epoch J2000); (3) Date of observation; (4) and (5): Number of exposures on target and integration time per exposure; (6) Average airmass during observation; and (7): Average image quality (seeing). (8) The measured S/N on the stacked cube between 6600 and 6800 Å (see text).

used 8 and 12 degrees of freedom for the multiplicative and additive polynomials, respectively (Emsellem et al. 2019). For the age and metallicity fits, we fixed the velocity and used no additive polynomials, but kept the 12th degree in the multiplicative polynomial (Fensch et al. 2019). Then we used the weights provided by pPXF to derive the mean metallicities and mean ages from the SSP models for each galaxy. Similarly, we calculated the stellar mass-to-light ratio from the weights given by pPXF and the photometric predictions from the eMILES library (Vazdekis et al. 2010) in the V-band. Figure 2 shows the spectra and the best pPXF fits for three dwarfs. To improve the fits, we masked the remaining sky lines, which were not removed by ZAP. The errors on the best-fit parameters were estimated with a Monte Carlo method where we reshuffle the residuals in a bootstrap approach. The 16 and 84 percent interval (1σ in frequentist statistics) give the uncertainty. The S/N per pixel is measured in a region between 6600 and 6800 Å devoid of strong absorption or emission lines. It is calculated as the mean fraction between the flux and the square root of the variance. The variance itself has to be multiplied with the χ^2 value estimated by pPXF.

A note on the velocity extraction of KK 197 and KKs 58. In Fahrion et al. (2020a) we derived for these two galaxies line-of-sight velocities of $643.2 \pm 3.5 \text{ km s}^{-1}$ and $482.6 \pm 12.6 \text{ km s}^{-1}$, respectively. This differs slightly from the values measured here, due to a different set of SSP models used, as well as different ways of extracting the spectra from the cube. However, the values here and the values in Fahrion et al. (2020a) are consistent within 1σ . The same goes for the metallicities and ages. In Fahrion et al. (2020a) we estimated a slightly more metal-rich ($-0.84 \pm 0.12 \text{ dex}$ and $-1.35 \pm 0.23 \text{ dex}$) and younger ($10 \pm 1.0 \text{ Gyr}$ and $\sim 7 \text{ Gyr}$) population than we estimate here. For the metallicity, this is within 3σ and 1σ , respectively. The age estimation from data with a low S/N is highly uncertain, therefore a discrepancy within a few Gyr is not uncommon.

2.2. Globular clusters and planetary nebulae detection

To search for any GCs, we identified all the point sources with Source Extractor and extracted their spectra. For this purpose, we created a 2D image by collapsing the cube along the wavelength axis. We then inspected all the individual spectra to create a catalog of GCs. Two of our galaxies – KKs 58 and KK 197 – have already been analyzed in Fahrion et al. (2020a). These two dSphs contain a NSC, and KK 197 furthermore hosts two GCs and an extended stellar association. Here, we find one new GC in KKs 55, which is also visible in *Hubble* Space Telescope (HST) images available for this galaxy. For the remaining dwarfs, the data is either too shallow or there are simply no GCs within the MUSE FOV.

Furthermore, we searched the MUSE cubes for planetary nebulae (PNe) that might serve as additional kinematic tracers. For this purpose, we derived a narrow band image for each galaxy at the expected redshifted position of the [OIII] $\lambda 5007 \text{ \AA}$ emission line. By subtracting this narrow-band image from a collapsed image of the nearby stellar continuum, PNe should stand out as residual point sources. Using this approach we detected one PN in KK 197 at the following location: 13:22:04.51/-42:32:14.09, which is 0.5 arcmin from the center of the galaxy. Its spectrum is shown in Fig. 5 indicating the location of typical emission lines shifted to the velocity of the object. Only the strongest emission lines are visible due to too low S/N. The other galaxies either contain no PNe within the MUSE FOV, or the data is too shallow to detect them.

3. Results

In this section, we discuss the overall properties of the stellar populations of the observed dwarf galaxies (Sect. 3.1). Our radial velocity measurements confirm the Cen A group membership for 12 out of 14 targets. Then, we look into their GC and PNe population (Sects. 3.2 and 3.3) and derive the velocity dispersion

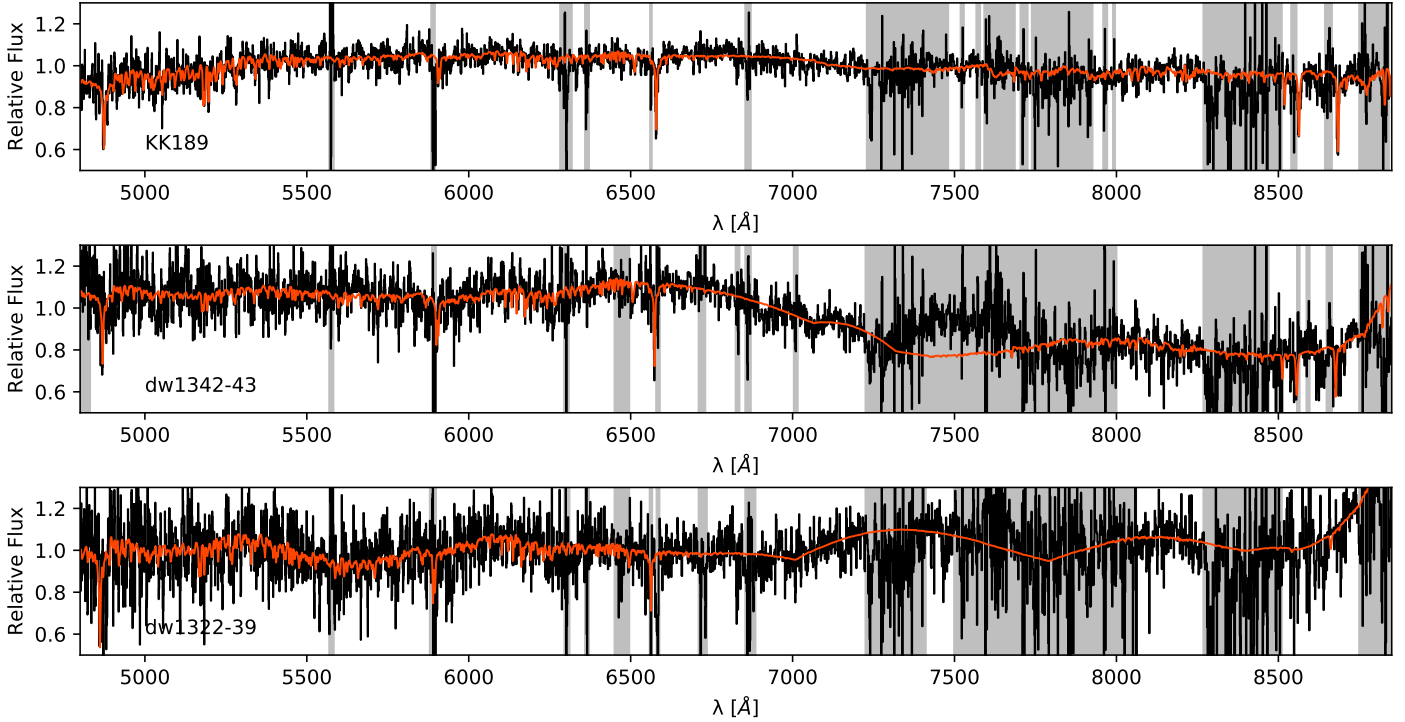


Fig. 2. Integrated MUSE spectra (black) of three example dwarf galaxies from our sample. The S/N decreases from top ($S/N = 28.5$) to bottom ($S/N = 11.9$) (see Table 1). The gray area are masked regions, the red lines correspond to the best-fit from pPXF. The spectra of the remaining galaxies are shown in Fig. C.1.

Table 2. Derived properties of the dwarf galaxies.

	KK 189	KKs 54	KK 197	KKs 55	dw1322-39	dw1323-40b	dw1323-40a	KK 203	dw1341-43	KKs 57	dw1342-43	KKs 58
v (km s ⁻¹)	752.6 ± 4.0	621.3 ± 10.6	642.7 ± 2.9	550.0 ± 23.7	656.3 ± 9.7	497.0 ± 12.4	450.0 ± 14.2	305.9 ± 9.5	636.4 ± 14.1	511.3 ± 16.8	510.3 ± 8.1	476.5 ± 5.2
[Fe/H] (dex)	-1.43 ^{+0.07} _{-0.07}	-1.81 ^{+0.07} _{-0.26}	-1.15 ^{+0.12} _{-0.01}	-1.14 ^{+0.04} _{-0.30}	-1.79 ^{+0.22} _{-0.13}	-1.84 ^{+0.01} _{-0.32}	-1.95 ^{+0.30} _{-0.14}	-1.75 ^{+0.11} _{-0.28}	-1.79 ^{+0.03} _{-0.33}	-1.90 ^{+0.07} _{-0.27}	-1.69 ^{+0.13} _{-0.19}	-1.49 ^{+0.07} _{-0.09}
Age (Gyr)	7.6 ^{+1.2} _{-1.2}	[7.4, 11.2]	11.7 ^{+2.2} _{-0.1}	5.8 ^{+3.3} _{-0.5}	11.5 ^{+2.5} _{-0.7}	[13.8, 14.0]	12.2 ^{+1.8} _{-3.7}	[7.0, 12.4]	[8.3, 11.7]	[10.7, 14.0]	12.2 ^{+1.8} _{-1.8}	14.0 ^{+0.0} _{-2.3}
M_V/L_V	1.4 ^{+0.1} _{-0.1}	[1.3, 1.8]	2.1 ^{+0.5} _{-0.0}	1.2 ^{+0.4} _{-0.1}	1.8 ^{+0.3} _{-0.1}	[2.1, 2.2]	1.9 ^{+0.3} _{-0.5}	2.1 ^{+0.0} _{-0.1}	[1.4, 1.9]	[1.6, 2.2]	1.9 ^{+0.2} _{-0.2}	2.2 ^{+0.0} _{-0.3}
M_V (mag)	-11.2	-10.4	-13.0	-12.6	-10.0	-10.0	-10.4	-11.7	-10.1	-10.6	-9.8	-11.9
r_{eff} (arcsec)	14.4	16.6	44.4	36.4	20.7	17.1	15.2	19.8	20.2	12.0	15.5	26.4
$\mu_{\text{eff},V}$ (mag/□)	24.5	25.6	24.8	25.5	25.9	26.1	25.4	24.6	26.2	24.8	25.5	24.6

Notes. The properties for M_V , r_{eff} , and $\mu_{\text{eff},V}$ were derived using the photometry from Jerjen et al. (2000) for KKs58, and from Müller et al. (2017) for the rest. No values for $\mu_{\text{eff},V}$ and r_{eff} are available in the literature for KK 203, so we derived it here ourselves (see Appendix A).

and dynamical mass of KK 197 (Sect. 3.4) using these discrete tracers. We also report the surprising discovery of a heart-shaped extended H α region in the dSph KK 203 (Sect. 3.5).

3.1. Properties of the stellar populations

The integrated spectra of the 12 dSphs (see, e.g., Fig. 2) display several absorption features and no strong emission lines, as expected for passive galaxies dominated by old stars. The velocities derived from these absorption lines are consistent with the velocity range of the Centaurus group (Müller et al. 2018a). The pPXF fits indicate that these spectra are consistent with old (6–14 Gyr) and metal poor ($-1.95 \lesssim [\text{Fe}/\text{H}] \lesssim -1.15$ dex) stellar populations. For an accurate estimation of the weighted mean ages of the stellar populations, however, we would need high S/Ns (see Fig. A.1 of Fahrion et al. 2019b for the required S/N for measuring velocities, metallicities, and ages with E-MILES SSP templates), which is not reached here. Nevertheless, we have estimated ages for all the objects and where pPXF did not converge to a single value, we give the 80% bounds. All the prop-

erties of the dwarfs are compiled in Table 2, but the mean stellar ages should be taken with a grain of salt. It is interesting to note that for the dwarf galaxy with one of the highest S/N – KK 203 – we find the youngest age (7.6 ± 1.2 Gyr). For two targets we measure strong emission lines, for which the derived velocities put them far in the background (see Appendix B).

Dwarf galaxies in the Local Group follow several scaling relations (Martin et al. 2008; Kirby et al. 2013). One of the most important is the stellar metallicity-luminosity relation. In Fig. 3 we investigate this relation for our 12 dSphs and compare them with a compilation of Local Group and nearby galaxies from McConnachie (2012), as well as with previously studied dwarfs in the Cen A group (Rejkuba et al. 2006; Cmojević et al. 2010, 2012, 2019; Müller et al. 2019b). We note that the mean metallicity for these different samples is based on several different techniques. The extended catalog from McConnachie (2012) includes metallicity measurements based on photometric methods such as RGB colors, isochrones fitting, or full CMD fitting, as well as spectroscopic metallicities from low-resolution Ca triplet or from spectral synthesis based on medium to high-resolution spectra.

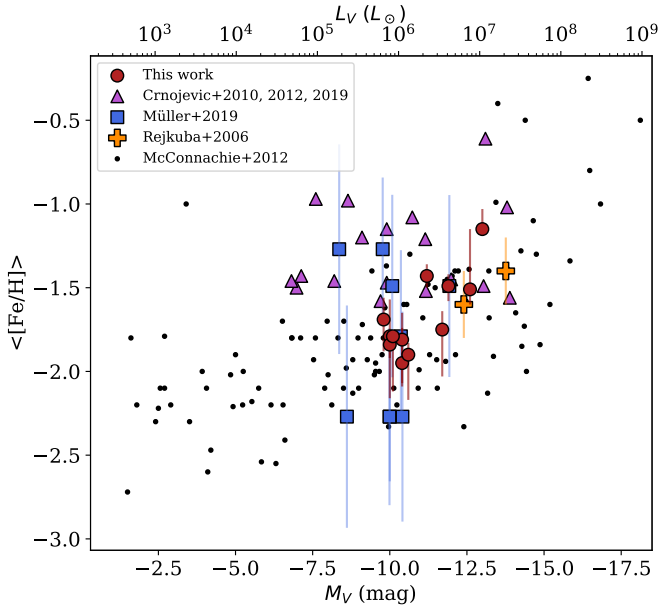


Fig. 3. Luminosity-metallicity relation for dwarf galaxies in the Cen A group (crosses, triangles, squares; Rejkuba et al. 2006; Crnojević et al. 2010, 2011b, 2019; Müller et al. 2019b) and Local Group (black dots, McConnachie 2012, from the updated online catalog, and are compiled from different sources, for example from Bellazzini et al. 2004; Martin et al. 2009; Correnti et al. 2009; Kirby et al. 2013; Torrealba et al. 2016; Hargis et al. 2016; Muñoz et al. 2018). The dwarfs from this work are indicated as red dots.

The latter measurements are based on observations of individual stars and it is interesting therefore to compare alongside with the mean metallicity of Cen A dwarfs obtained from resolved stellar population studies (Rejkuba et al. 2006; Crnojević et al. 2010, 2012, 2019; Müller et al. 2019b), as well as integrated light analysis with MUSE. The dwarf galaxies of the Cen A group follow the same stellar metallicity-luminosity relation as dwarf galaxies in the Local Group (Fig. 3). While the MUSE spectroscopic metallicities lie exactly on top of the McConnachie (2012) metallicity-luminosity relation, there is a much larger scatter for photometric measurements. This is not surprising because at the distance of the Cen A group, only few magnitudes of the upper RGB can be resolved, and from optical photometry it is impossible to distinguish between 5 and 10 Gyr old RGB stars. The age-metallicity degeneracy and possibly incorrect assumptions for the uniform old (~ 10 Gyr) age of the population lead to larger uncertainties in photometric metallicities. Furthermore, a systematic offset in metallicity scale may result from a choice of a specific isochrone set or empirical RGB calibration (Rejkuba et al. 2014; Streich et al. 2014).

3.2. Globular clusters properties

In our sample of 12 dwarf galaxies, three host stellar clusters: KK 197, KKs 55, and KKs 58. Fahrion et al. (2020a) analyzed two GCs, one NSC, and one extended stellar association in KK 197 and one NSC in KK 58. Around KKs 55, Georgiev et al. (2010) found one GC based on deep HST data that lies outside the MUSE FOV. For this galaxy, we discovered an additional GC in the MUSE data that is visible in the HST data as well, although it can easily be confused with a background galaxy shining through KKs 55. Its spectrum unambiguously

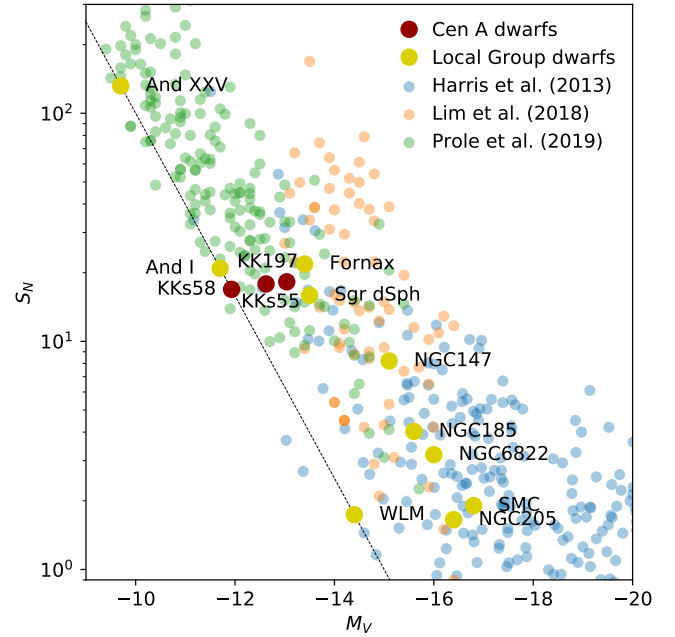


Fig. 4. Specific frequency of the Cen A dwarfs (big red dots) compared to other galaxies. Blue dots are nearby galaxies from Harris et al. (2013), orange dots are Coma dwarf galaxies (Lim et al. 2018), and green dots are Fornax dwarf galaxies (Prole et al. 2019). The Local Group dwarfs are indicated with big yellow dots (Grebel 2016; Cusano et al. 2016; Caldwell et al. 2017). The dashed line indicates the specific frequency of an object with one GC. The specific frequencies for the Coma and Fornax dwarfs were estimated on a statistical basis, and often they are consistent with zero within the uncertainties.

confirms the association with the dwarf galaxy. The coordinates for this new GC are RA = 13:22:13.869 and Dec = $-42:44:05.04$. Performing simple aperture photometry on the HST data we derive apparent magnitudes of $M_V = 22.8 \pm 0.1$ mag and $M_I = 21.8 \pm 0.1$ mag in the Vega system. With a distance modulus of 27.93 mag (Karachentsev et al. 2013), this gives extinction corrected absolute magnitudes of $M_V = -5.5$ mag and $M_I = -6.2$ mag, respectively, with a color of $(V - I)_0 = 0.7$ mag. From the MUSE spectrum, we determined a velocity of 531.4 ± 15.4 km s $^{-1}$, a metallicity of $-1.50^{+0.34}_{-0.07}$ dex, a mean age of $12.9^{+1.4}_{-2.5}$ Gyr, and a mass-to-light ratio of $2.1^{+0.3}_{-0.4} M_\odot/L_\odot$. This GC seems to be more metal-poor than the stellar population of its host dwarf galaxy ($[M/H] = -1.14^{+0.04}_{-0.30}$ dex).

To characterize the GC systems, we derived the specific frequency $S_N = N_{GC} \times 10^{0.4(M_V+15)}$ (Harris & van den Bergh 1981) for each dwarf. The results are presented in Fig. 4. Where no GC is detected, S_N is assigned a value of zero, although it is possible that some GCs are outside the MUSE FOV or are too faint to be detected in our data. For KK 197 and KKs 58, the S_N are 18.2 and 16.9, respectively (Fahrion et al. 2020a), and for KKs 55 it is 17.9. These numbers are compatible with the specific frequencies of dwarf galaxies from the Local Group (Grebel 2016) and other nearby dwarf galaxies (Georgiev et al. 2010; Harris et al. 2013), as well as dwarf galaxies in clusters (Lim et al. 2018; Prole et al. 2019; Saifollahi et al. 2021), but we note that the S_N has a significant scatter in the classical dwarf galaxy regime.

3.3. Planetary nebula properties

Do we expect to find PNe in our dwarf galaxies? Considering the small number of PNe in Local Group dwarfs, we

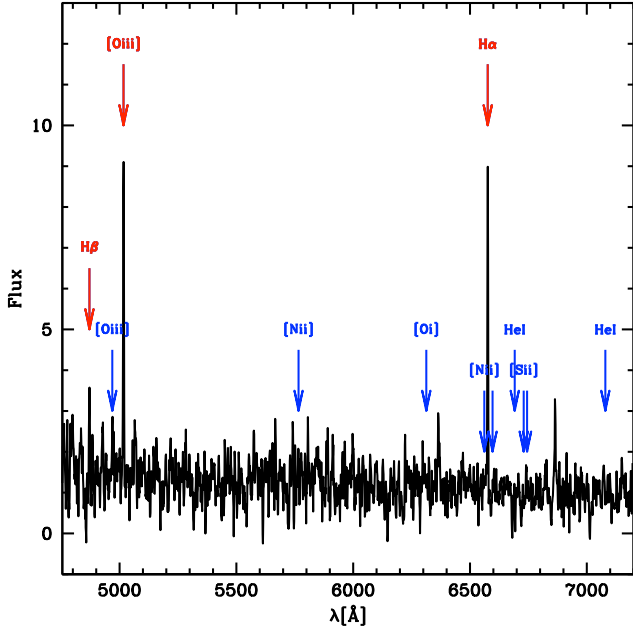


Fig. 5. MUSE spectrum of the PN in KK 197. The red and blue arrows indicate typical emission lines of PNe of which only the strongest ones ($H\alpha$, 5007 Å [OIII]) and possibly $H\beta$ are detected, marked in red. The spectra were slightly smoothed with a three-point boxcar filter.

expect very few PNe in our sample (Reid 2015). The number of PNe scales with the total sampled luminosity as $N_{\text{PN}} = \alpha L_{\text{bol}}$ (Buzzoni et al. 2006). There is a considerable uncertainty in theoretical predictions for the value of α , which depends on the PN lifetime and specific evolutionary flux (i.e., how many PNe are produced per simple stellar population luminosity), which in turn depends on the star formation rate and metallicity of the population. The Local Group PN census confirms theoretical expectations that metal-poor populations host fewer PNe. For example for the SMC metallicity of ~ -1.25 dex Reid (2015) derived $\alpha = 1 \text{ PN}/4.6 \times 10^6 L_{\odot}$. Some of our dwarfs are significantly more metal-poor than the SMC and similar to Local Group dSph that have no known PN. Hence, it is not surprising that we only detect one PN, which is potentially associated with the brightest dwarf in our sample: KK 197.

In Fig. 5 we present the spectrum for this PN and indicate the typical emission lines of PNe. There is clear [OIII] and $H\alpha$ emission and likely $H\beta$ emission. The line-of-sight velocity of the PN from the emission lines ($v_{\text{KK197,PN}} = 588.42 \pm 2.5 \text{ km s}^{-1}$) differs by about 55 km s^{-1} from the systemic velocity of KK 197 measured from the stellar absorption lines in the same datacube ($642.7 \pm 2.9 \text{ km s}^{-1}$), which may be interpreted as a real physical association. However, it is also possible that the PN is associated with Cen A itself and appears in the MUSE FOV only by chance, as the PNe population of the Cen A halo extends to the position of KK 197 (Walsh et al. 2015). With an offset of $\sim 50 \text{ km s}^{-1}$ to the mean of the PNe population ($v_{\text{Cen A}} = 536.7 \pm 4.2 \text{ km s}^{-1}$) it is entirely plausible that the PN is an interloper, since the standard deviation of the 1107 PNe studied in Walsh et al. (2015) is 141 km s^{-1} .

3.4. Internal dynamics of KK 197

The simultaneous extraction of the spectrum of the stellar body of a galaxy and the spectra of its associated star clusters makes it

Table 3. Kinematic tracers for the mass derivation of KK 197. The velocities are from Fahrion et al. (2020a) for the stellar clusters and from here for the PN.

Name	v (km s^{-1})	v_{err} (km s^{-1})
KK197	642.7	2.9
KK197-NSC	635.4	1.5
KK197-1	636.4	16
KK197-3	642.6	3.8
KK197-SA	619.3	10.3
KK197-PN	588.4	2.5

possible to estimate the galaxy’s velocity dispersion³ and therefore probe its dynamical mass and dark matter content (e.g., van Dokkum et al. 2018, 2019; Martin et al. 2018; Müller et al. 2020). More and more such studies are now conducted in the dwarf galaxy regime. A reliable dynamical mass estimate, however, requires the presence of multiple kinematic tracers of the underlying gravitational potential, such as GCs or PNe (Côté et al. 2001; Pota et al. 2013; Forbes et al. 2017; Laporte et al. 2019; Fahrion et al. 2020b). For the brightest galaxy in our sample – KK 197 – five discrete tracers are available. For the detailed methodology, we refer to Müller et al. (2020). The tracers are listed in Table 3.

In short, we used a Markov chain Monte Carlo (MCMC) approach with the logarithmic likelihood function given as

$$\log \mathcal{L} = \sum_{i=1}^N \log \left(\frac{1}{\sqrt{2\pi}\sigma_{\text{obs}}} \right) - \frac{(v_{\text{obs},i} - v_{\text{sys}})^2}{2\sigma_{\text{obs}}^2}, \quad (1)$$

where N is the number of tracers, $v_{\text{obs},i}$ is the observed line-of-sight velocity of an individual tracer i , v_{sys} is the systemic velocity of the whole system, and σ_{obs} is the observed velocity dispersion given by a combination of the true velocity dispersion σ_{int} and the observational uncertainties:

$$\sigma_{\text{obs}}^2 = \sigma_{\text{int}}^2 + \delta_{v,i}^2. \quad (2)$$

The two variables v_{sys} and σ_{int} are the parameters we are interested in. A non-informative prior is imposed to suppress a too small velocity dispersion (Agnello & Bruun, in prep.):

$$P(\theta) = \frac{\sigma_{\text{int}}}{(\sigma_{\text{int}}^2 + \epsilon^2)^{3/2}}, \quad (3)$$

where ϵ is the mean velocity error. We used 100 walkers with a chain length of 10 000 each. The sampled posterior distribution is shown in Fig. 6 for two different cases: considering the newly discovered PN bound to KK 197 (left, with $N = 5$) or assuming it is an interloper associated with Cen A (right, with $N = 4$).

From a dynamical perspective, it is very unlikely that the PN belongs to KK 197 because the line-of-sight velocity difference of $\sim 55 \text{ km s}^{-1}$ to the putative host is comparable to the inferred escape velocity $V_{\text{esc}} \approx \sqrt{2} \sqrt{3} \sigma_{\text{int}}$ when the PN is included in the estimate of σ_{int} ($V_{\text{esc}} \approx 62 \text{ km s}^{-1}$) and much larger when the PN is excluded ($V_{\text{esc}} \approx 21 \text{ km s}^{-1}$). Moreover, the systemic velocity

³ To directly measure the velocity dispersion of the stellar body, we would need deeper data. See for example Emsellem et al. (2019) for a study with MUSE of the velocity dispersion measured on the spectra of a comparable dwarf galaxy.

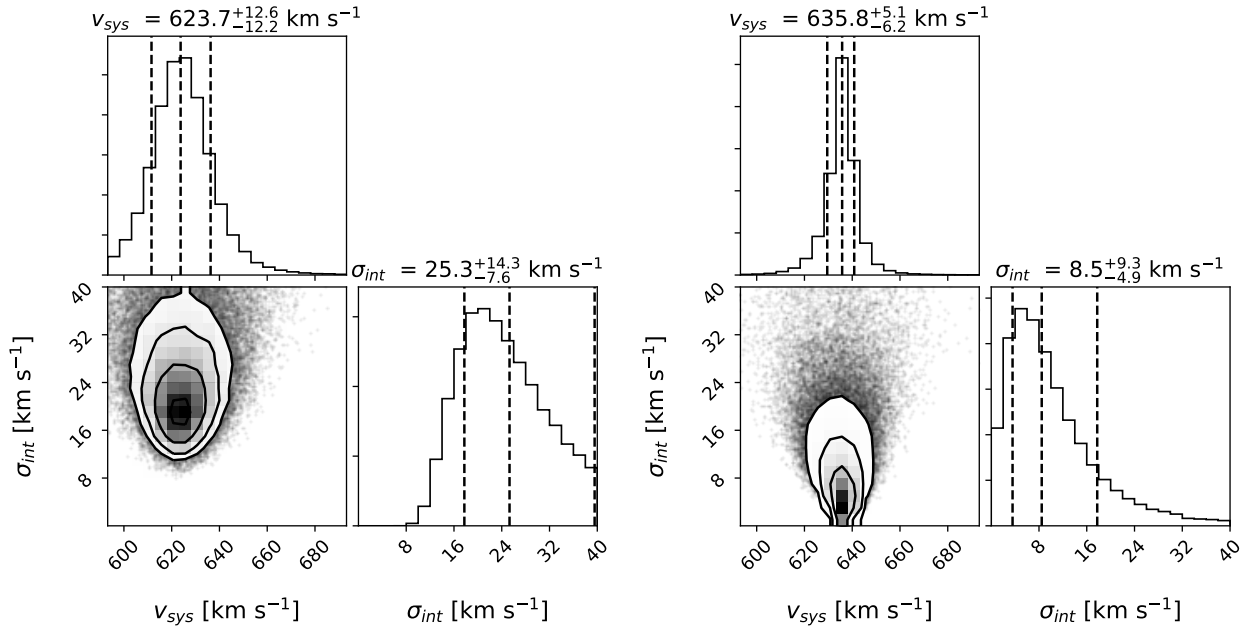


Fig. 6. Posterior distribution from the MCMC analysis of the velocity dispersion of KK 197, as well as the systemic velocity of the tracers. *Left* is the estimation including the PN as tracer, *right* without including it. The three dashed lines indicate the 16, 50, and 84 percentiles, which correspond to the upper and lower uncertainty boundaries, and the best parameter estimation (i.e., the median).

of KK 197 from the stellar absorption lines ($643.2 \pm 3.5 \text{ km s}^{-1}$) is closer to the maximum-likelihood value of v_{sys} when the PN is excluded ($635.8^{+5.1}_{-6.2} \text{ km s}^{-1}$) rather than when it is included ($623.7^{+12.6}_{-12.2} \text{ km s}^{-1}$). In the following, for the sake of completeness, we provide dynamical mass measurements using both values of σ_{int} but the one excluding the PN should be considered more reliable despite the lower number of kinematic tracers.

From the intrinsic velocity dispersion, the dynamical mass enclosed within the de-projected half light radius $r_{1/2}$ can be estimated using the following formula (Wolf et al. 2010):

$$M_{\text{dyn}}(r_{1/2}) = \frac{4r_{\text{eff}}\sigma_{\text{int}}^2}{G} \quad (4)$$

with $r_{1/2} = 4/3r_{\text{eff}}$. The resulting dynamical mass within $r_{1/2}$ is $M_{\text{dyn}} = 0.5^{+1.8}_{-0.4} \times 10^8 M_{\odot}$ considering only the GCs and $4.9^{+7.1}_{-2.5} \times 10^8 M_{\odot}$ including the uncertain PN. To estimate the dynamical mass-to-light ratio, we transform the V-band magnitude of KK 197 into solar luminosities. This gives $M_{\text{dyn}}/L_V = 4.0^{+13.8}_{-3.3} M_{\odot}/L_{\odot}$ and $36.6^{+53.2}_{-18.7} M_{\odot}/L_{\odot}$ excluding and including the PN, respectively.

The dynamical mass-to-light ratios of galaxies are known to anti-correlate with galaxy luminosity and surface brightness (e.g., McGaugh & de Blok 1998). A more comprehensive representation of galaxy dynamics is offered by the radial acceleration relation (RAR, Lelli et al. 2017), in which the observed kinematic acceleration g_{obs} is compared to the Newtonian gravitational field g_{bar} from the baryonic mass distribution. If the data follows the line of unity, the observed dynamics can be fully explained by the visible matter. If the observed acceleration is larger than the one caused by the baryons, an additional gravitational component (i.e., dark matter), is necessary.

For spherical, pressure-supported systems, the observed acceleration can be computed as

$$g_{\text{obs}} = \frac{3\sigma_{\text{int}}^2}{r_{1/2}}, \quad (5)$$

and the baryonic gravitational field is given by

$$g_{\text{bar}} = \frac{\Gamma_V G L_V}{2r_{1/2}^2}, \quad (6)$$

where Γ_V is the stellar mass-to-light ratio. From the spectroscopy of KK 197, we measured $\Gamma_V = 2.3^{+0.3}_{-0.3}$. Figure 7 shows the location of KK 197 on the RAR established using rotation-supported disk galaxies (gray color scale) together with measurements of other pressure-supported dwarf galaxies from the literature. KK 197 follows the same RAR as rotation-supported galaxies within 2σ , independently of whether we include or exclude the PN in the estimate of the velocity dispersion.

The dynamics of dwarf galaxies can be used to test alternative gravity models like modified Newtonian dynamics (MOND, Milgrom 1983, see also its review by Famaey & McGaugh 2012). In MOND, rather than adding dark matter to a galaxy to explain the high dynamical mass-to-light ratio, the law of gravity is modified such that the baryons produce the dark matter-like behavior. Due to the nonlinear modification of the Poisson equation in MOND, a so-called external field effect (EFE, see e.g., Haggi et al. 2019) emerges when the galaxy is embedded in an external gravitational field. If the internal acceleration is stronger than the external one, the galaxy can be treated as in isolation, however in the opposite case the EFE has to be considered and it will lower the expected internal acceleration (Kroupa et al. 2018; Famaey et al. 2018).

Following the methodology presented in Müller et al. (2019c), we calculated the velocity dispersion for KK 197 as a function of its 3D separation to Cen A. The measured separation is $r_{3D} = 145 \pm 22 \text{ kpc}$ (Karachentsev et al. 2007, 2013). In Fig. 8, we present the MOND prediction and compare it to the observations. In isolation, the expected velocity dispersion is $\sigma_{\text{MOND,isolated}} = 13.2^{+2.5}_{-2.1} \text{ km s}^{-1}$. However, at this 3D separation from Cen A, the galaxy is already affected by the EFE, lowering the expected velocity dispersion to $\sigma_{\text{MOND,EFE}} = 11.5^{+4.5}_{-3.0} \text{ km s}^{-1}$. This prediction is in close agreement with the measured velocity dispersion of $8.5^{+9.3}_{-4.9} \text{ km s}^{-1}$ when the PN is excluded, as it is

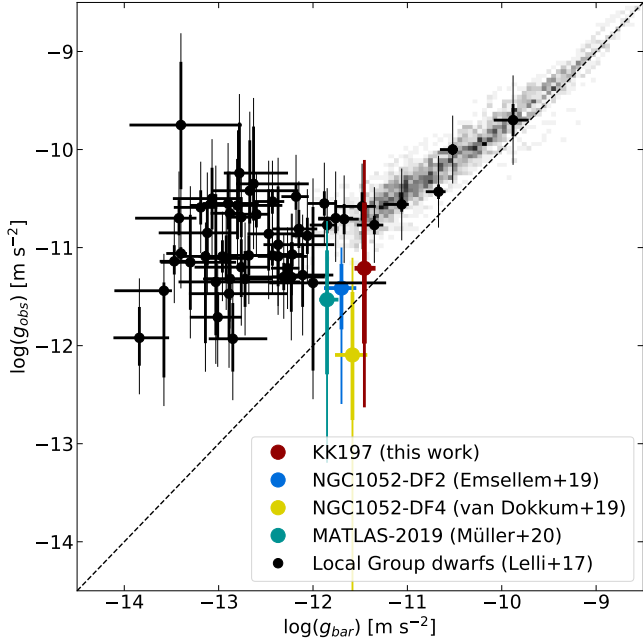


Fig. 7. Radial acceleration relation of galaxies. The dashed line corresponds to unity, meaning that the baryonic acceleration (x -axis) is equal to the observed acceleration in the system (y -axis). The gray scale represents ~ 2700 spatially resolved measurements in rotationally supported galaxies (spirals and dIrrs, see [McGaugh et al. 2016](#)). The black dots correspond to pressure-supported dwarf galaxies in the Local Group as compiled in [Lelli et al. \(2017\)](#) and come from different sources (e.g., [Simon & Geha 2007](#); [Mateo et al. 2008](#); [Koch et al. 2009](#); [Walker et al. 2009](#); [Geha et al. 2010](#); [Tollerud et al. 2012](#); [Collins et al. 2013, 2015](#); [Martin et al. 2014](#)). The cyan dot represents MATLAS-2019 ([Müller et al. 2020](#)). The blue and yellow lines are two so-called ultra diffuse galaxies: NGC 1052-DF2 ([Danieli et al. 2019](#)) and NGC 1052-DF4 ([van Dokkum et al. 2019](#)). The red dot shows our new measurements for KK 197. The thick and thin lines are the 1 and 2σ uncertainties, respectively.

likely associated with Cen A. When the PN is included in the fit, the measured dispersion increases to $25.2^{+14.3}_{-7.6}$ km s $^{-1}$ (i.e., a 2σ tension with the predicted MOND value).

3.5. $H\alpha$ emission of KK 203

Unexpectedly, in the spectrum of one of the dSphs (KK 203) we detected conspicuous $H\alpha$ emission, forming an extended heart-shaped region around the galaxy (see [Fig. 9](#)). This seems to be a continuous ring, somewhat off-centered from the galaxy, with a diameter of $\sim 24''$ (440 pc). On average, the $H\alpha$ velocities obtained from fitting individual spaxels are well in agreement with the systemic velocity of KK 203, making their physical association extremely likely. Only $H\alpha$ and perhaps $H\beta$ emissions are detected forming this ring, other potential emission lines do not stand out above the continuum of the galaxy (see [Fig. 10](#)).

Where does this $H\alpha$ emission come from? $H\alpha$ emission is typically associated with the presence of star formation, AGN, or shocks. In late-type spiral galaxies, on the order of 50% of $H\alpha$ emission is coming from a warm diffuse component of the interstellar medium (ISM, [Oey et al. 2007](#)), which can be ionized by photons leaking from HII regions, evolved field stars, shocks, or cosmic rays. This so-called diffuse interstellar gas (DIG) or warm ionized medium is also observed in early-type galaxies ([Phillips et al. 1986](#); [Martel et al. 2004](#); [Jaffé et al. 2014](#)).

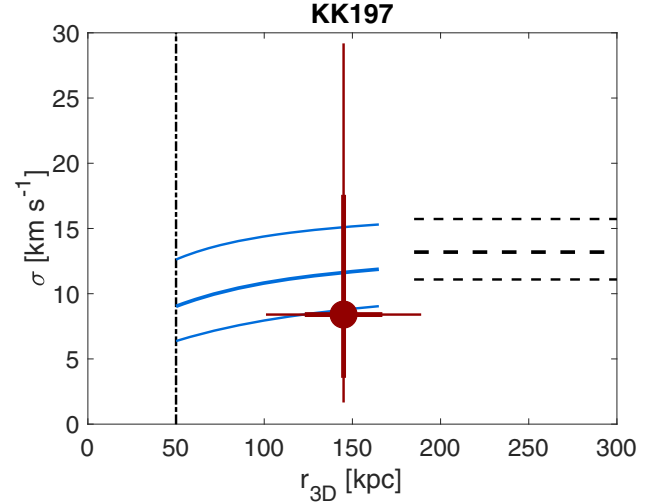


Fig. 8. Predicted MOND velocity dispersion for KK 197 as a function of its 3D separation to Cen A. The horizontal dashed lines show the MOND prediction (and its 1σ uncertainty) for the isolated case, while blue lines correspond to the MOND prediction considering the EFE from Cen A. The red dot is the measured value considering the stellar clusters. The 1σ and 2σ uncertainties are represented by the thick and thin red lines.

The DIG has a lower electron density, higher electron temperature, and enhanced line ratios between collisionally excited and recombination lines when compared to HII regions. Unfortunately, the lack of unambiguous detection of forbidden emission lines such as [SII] and [NII] within the same heart-shaped ring region means that we cannot use the usual diagnostics based on integrated spectra ([Levesque et al. 2010](#); [Kewley et al. 2019](#)).

There is no detection of neutral hydrogen in HIPASS at the location of KK 203 ([Barnes et al. 2001](#)), so the amount of cold gas (the fuel for any potential star formation) is rather low as expected for a dSph galaxy. However, the non-detection might also be due to the fact that the dwarf is smaller than the HIPASS spatial resolution element (15 arcmin) and that the HIPASS detection limit is around $M_{\text{HI}} \approx 10^7 M_{\odot}$ for dwarf galaxies in the Centaurus group ([Müller et al. 2017](#)).

There are no obvious individual HII regions detected in the MUSE data-cube. To ensure that we are not missing a possible low fraction of young or intermediate-age stars due to relatively low S/N of our spectroscopic data we carefully examined the available optical imaging from the HST archive. Based on DOLPHOT PSF fitting photometry ([Dolphin 2016](#)) applied to the ACS at HST images (HST program 13442, PI: Tully) we derive $F606W$ (wide V -band) versus $F606W - F814W$ (equivalent to $V - I$) color-magnitude diagram (CMD) shown in [Fig. 11](#). We first verified that the bulk of the stars in the CMD is well fit with an old and metal-poor population by overlaying 14 Gyr BASTI solar-scaled isochrones ([Pietrinferni et al. 2004](#)) with metallicities that bracket the mean value derived from the MUSE spectrum. We find an excellent agreement between spectroscopic metallicity from the integrated MUSE spectrum and the photometric metallicity from the color of the red giant branch (RGB) sequence.

The foreground MW stars are primarily found at $F606W - F814W \gtrsim 1.1$, which is redder than most of the KK 203 stars, but some compact blue galaxies may contaminate star counts at $F606W - F814W \lesssim 0.2$ and $F606W \gtrsim 25.5$, where young stars of KK 203 are located. We cleaned the CMD from foreground/background stellar sources by applying

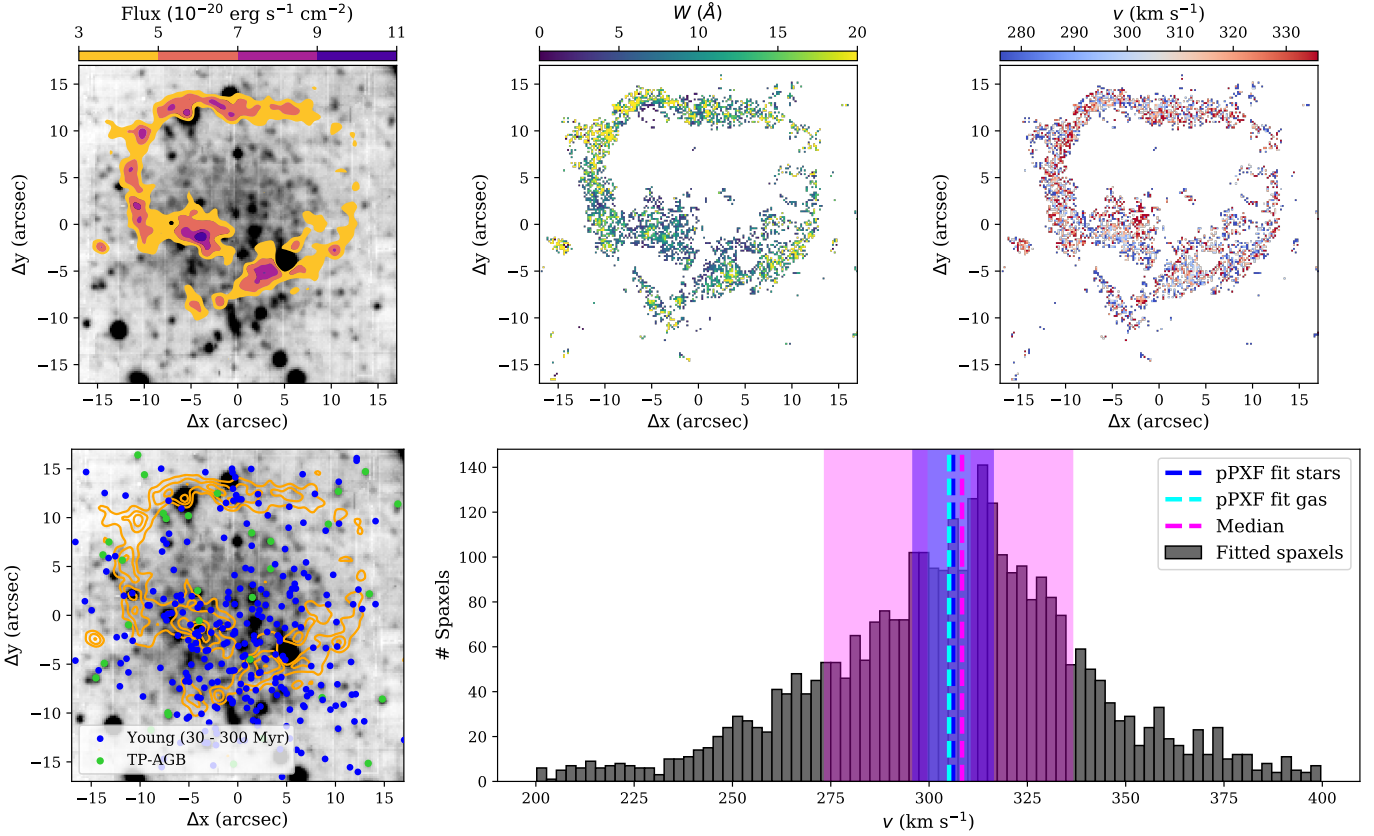


Fig. 9. Dwarf galaxy KK203 with its $H\alpha$ emission. *Top left:* white-light image of KK203 with $H\alpha$ intensity contours. The contours refer to the residual $H\alpha$ emission, created by subtracting a continuum image from a narrow-band $H\alpha$ image obtained from the MUSE cube. *Top-middle and top-right:* equivalent width and line-of-sight velocity of the $H\alpha$ emission, obtained from fitting spaxels with a Gaussian curve. *Bottom-left:* white light image with $H\alpha$ contour and young supergiants (blue) and TP-AGB stars overplotted (see Fig. 11 for the selection). RGB stars are distributed randomly over the galaxy and are not shown here. *Bottom-right:* histogram of line-of-sight velocities. The median with 1σ uncertainties is highlighted in pink, light and dark blue refer to the results from the pPXF fit of the stellar and gas component to the integrated spectrum.

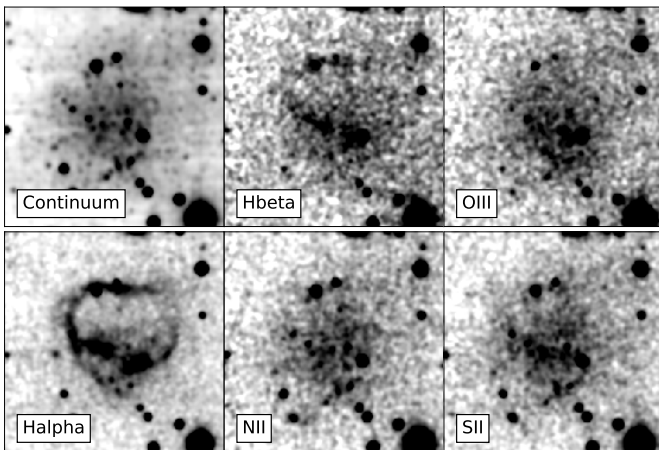


Fig. 10. Dwarf galaxy KK203 and its emission regions. The images were produced as the sum of the MUSE cube for the continuum panel, and as single slices at the corresponding wavelengths for the emissions. To enhance the features, a small Gaussian convolution was applied.

statistical subtraction from a neighboring patch of the sky selected in the same image (see Müller et al. 2018b, for more details). The cleaned CMD still presents an excess of blue stars. The detection limit at $F814W \sim 27$ mag, visible as a diagonal limit in the $F606W$ versus $F606W - F814W$ CMD (right panel

of Fig. 11), implies that main sequence stars with ages older than ~ 30 Myr are not observable. The right panel of Fig. 11 shows the statistically cleaned CMD with the solar-scaled BASTI isochrones for $[M/H] = -1.8$ dex and a range of ages. It shows that evolved supergiants younger than $\lesssim 300$ Myr can be detected. Their short evolutionary lifetime leads to a relatively sparsely populated CMD area on the blue side of the RGB. We verified by overplotting more metal-rich isochrones that there are likely no stars younger than ~ 30 Myr present in KK203 and that stars indicated in the blue selection box span a range of ages between 30 and 300 Myr. Due to the age-metallicity degeneracy in the VI photometric bands it is not possible to assign unambiguous ages to these blue stars. Deeper observations are needed to constrain the metallicity and thus derive more accurate ages for at least a handful of brightest supergiants. Such data could be obtained with adaptive optics assisted MUSE observations (e.g., Della Bruna et al. 2020).

In Fig. 11 we identify regions of the CMD according to age: the RGB (red) contains predominantly old stars, the green area indicates the region where intermediate-age thermally pulsing asymptotic giant branch (TP-AGB) stars are located, and we show young supergiants in the blue selection box. After selecting stars on the statistically cleaned CMD of KK203 according to region, we plot them on top of the MUSE white-light cube image with color coding of dots reflecting the CMD region color (except for RGB stars), and overplotting in cyan contours the $H\alpha$ gas (bottom left panel in Fig. 9). The youngest stars are most

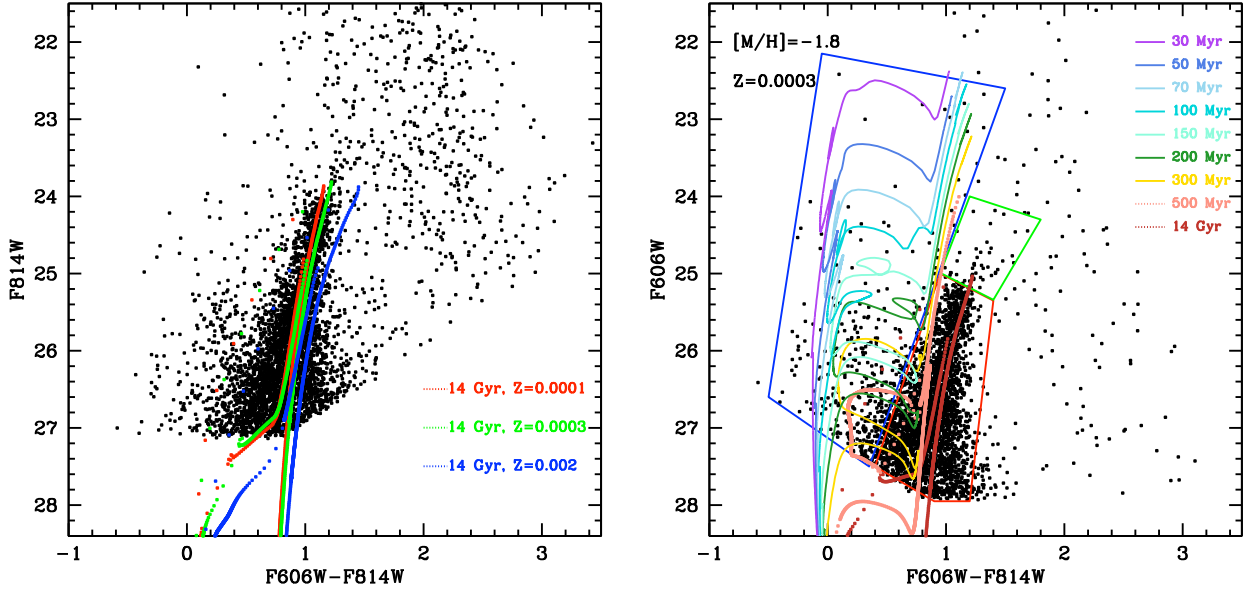


Fig. 11. *Left panel:* $F814W$ versus $F606W - F814W$ color-magnitude diagram of KK 203 from the ACS HST imaging showing all sources identified as bona fide stars by the DOLPHOT PSF fitting routine. Overplotted are three BASTI isochrones for a 14 Gyr old population and metallicities as indicated in the legend. *Right panel:* statistically cleaned CMD, this time with $F606W$ on y-axis to emphasize the presence of young blue stars with ages ranging between 30–300 Myr (blue box). The areas of the CMD where the old RGB stars (red) and intermediate-age thermally pulsing asymptotic giant branch (TP-AGB) stars (green) are located are also indicated. A set of BASTI solar-scaled isochrones with the range of ages indicated in the legend does not include the TP-AGB phase.

centrally concentrated and are displaced southwards with respect to the galaxy center. Our conclusion from the analysis of the HST data is that, although there are some young stars with ages between 30 and 300 Myr, the low-level star formation is likely not sufficient to photoionize the extended $H\alpha$ emission in a ring surrounding KK 203.

Another common source of $H\alpha$ emission in massive galaxies is represented by supermassive black holes powering active galactic nuclei (AGN). In this case, however, we would expect the $H\alpha$ emission to be concentrated toward the galaxy center rather than forming an extended ring. Unfortunately, given the low metallicity of the galaxy, we do not detect oxygen and nitrogen emission lines, which could have been used to build BPT diagrams (Baldwin et al. 1981) and study the nature of the radiation field.

Another possibility is that the $H\alpha$ emission comes from winds of AGB and post-AGB stars or young supergiants. For this purpose, we have used the HST photometry of this galaxy, plotted all potential AGB stars (extending the TRGB to brighter magnitudes) and post-AGB and supergiant stars (bluer than the RGB branch) over the collapsed MUSE cube, and compared it to the $H\alpha$ emission. The candidate AGB stars are roughly uniformly distributed over the galaxy, whereas the candidate bluer stars are somewhat clustered toward the southwest, overlaying at least partially with the southern part of the $H\alpha$ ring. However, there is no clear correlation between these stars and the $H\alpha$ ring, especially for the northern part. If we reverse the approach and use the $H\alpha$ ring as a mask to select the stars in the CMD, mainly RGB stars are selected. This indicates that there is no evidence for a connection between AGB or post-AGB stars and the $H\alpha$ ring.

Could the $H\alpha$ emission have an external or environmental origin? One possibility is that some interstellar gas in KK 203 is excited by an exterior radiation field, namely that of Cen A. The 3D separation between Cen A and KK 203 is ≈ 230 kpc. This seems to be at a distance from Cen A where the radiation den-

sity is too low for exciting/shocking the gas in the dwarf. Perhaps KK 203 had a closer passage to Cen A in the past and its interstellar medium was tidally shocked, so what we see in $H\alpha$ is the aftereffect of this encounter. A more speculative idea is that KK 203 has accreted a much smaller dwarf galaxy or DM halo with some diffuse ionized gas, so the ring would represent a gaseous stream.

Yet another explanation could be that we see an old supernova remnant (SNR). Karachentsev & Kaisin (2020) conducted an $H\alpha$ survey in dwarf galaxies with the 6 m BTA telescope of the Special Astrophysical Observatory. In their sample of 309 irregular and transitional type dwarf galaxies a number of different emission features were uncovered. Among them, there were so-called B-bubbles, which they describe as ring-like structures similar to SNRs. About 17% percent of their dwarf galaxies contained such B-bubbles with an average diameter of 120–240 pc, which is somewhat smaller than what we observe here (we note though that Karachentsev & Kaisin 2020 simply assumed a distance of 5 Mpc for all their targets and transformed the average angular size into a physical one, but also none of them is as large as the ring around KK 203, priv. comm. with I. Karachentsev). Evans et al. (2019) found two bubbles reminiscent of the one discovered here in the nearby dIrr Leo P (see their Fig. 10). To confirm whether this heart-shaped ring in KK 203 is an SNR, one would need to use the emission line ratios as diagnostics (Moumen et al. 2019), for which our current observations are too shallow. Moreover, given the low metallicity of the system, it is unclear whether deeper observations could be able to detect other gas emission lines beyond the Balmer series of atomic hydrogen. An SNR is the most satisfactory explanation for the following reason. Assuming that the SNR expanded with a constant velocity of 100 km s^{-1} (Kirshner & Taylor 1976), it would have needed 4×10^6 years to expand into its current form. This is consistent with the age of some of the brightest blue and red supergiants observed in the HST CMD (right panel of Fig. 11).

4. Summary and conclusions

We used MUSE spectroscopic observations to study the properties of a sample of dSphs in the Cen A galaxy group. Out of the 14 targeted objects, only two were revealed to be background galaxies based on their redshifts of ~ 0.01 . The remaining galaxies have been confirmed as Cen A members based on their line-of-sight velocities. We found the following results:

1. The integrated spectra of these 12 dSphs are consistent with old and metal-poor stellar populations, as expected from observations of dSphs in the Local Group. Moreover, the dSphs in the Cen A group follow a similar stellar metallicity-luminosity relation as dwarf galaxies in the Local Group.
2. For the three brightest dSphs in our sample (KK 197, KKs 55 and KKs 58), we found associated GCs. The specific frequency of GCs for these three dwarfs is around 18, which falls on the expected range from previous studies of other nearby galaxies.
3. We found a PN near the dwarf galaxy KK 197, revealed by its strong [OIII] and $H\alpha$ emission lines. It is quite likely, however, that this PN belongs to the outer halo of Cen A based on dynamical considerations.
4. For the brightest dSph – KK 197 – we estimated the intrinsic velocity dispersion using discrete tracers. Depending on whether the PN is considered or not, the velocity dispersion ranges from 8.5 to 25.3 km s^{-1} and the corresponding dynamical mass-to-light ratio from ~ 4 to $\sim 37 M_{\odot}/L_{\odot}$.
5. KK 197 lies on the same radial acceleration relation of rotationally supported galaxies within the errors. The measured velocity dispersion also agrees with the MOND prediction.
6. For one of our dSphs – KK 203 – we found a surprising $H\alpha$ emission, which forms a 400 pc wide, heart-shaped ring. The $H\alpha$ emission is not powered by recent star-formation. Its origin remains unclear but several possibilities are discussed, including a central supermassive black hole, AGB and post-AGB stars, a $\sim 40 \text{ Myr}$ old supernova remnant, or past interaction/accretion events. Our favorite interpretation is that $H\alpha$ is powered by an SNR, but deeper data are necessary to establish that on a firmer ground.

In a companion paper, we use the measured line-of-sight velocities of these 12 dSphs to study the overall dynamics of the Cen A group and, in particular, to confirm or disprove the presence of a rotating satellite system (Müller et al. 2018a).

Acknowledgements. We thank the referee for the constructive report, which helped to clarify and improve the manuscript. O.M. is grateful to the Swiss National Science Foundation for financial support. The authors thank Aku Venhola, and Yvez Revaz for the interesting discussions on the $H\alpha$ content of KK 203. This work has made use of BaSTI web tools. M.S.P. and O.M. thank the Deutscher Akademischer Austauschdienst for PPP grant 57512596 funded by the Bundesministerium für Bildung und Forschung, and the Partenariat Hubert Curien (PHC) for PROCOPE project 44677UE. M.S.P. thanks the Klaus Tschira Stiftung and German Scholars Organization for support via a KT Boost Fund. G.S.A. acknowledges support for this work provided by NASA through grant number HST-SNAP-15922 from the Space Telescope Science Institute. Based on observations made with the NASA/ESA Hubble Space Telescope, obtained from the data archive at the Space Telescope Science Institute. STScI is operated by the Association of Universities for Research in Astronomy, Inc. under NASA contract NAS 5-26555.

References

Bacon, R., Accardo, M., Adjali, L., et al. 2010, in *Ground-based and Airborne Instrumentation for Astronomy III*, Proc. SPIE, 7735, 773508
 Baldwin, J. A., Phillips, M. M., & Terlevich, R. 1981, *PASP*, 93, 5
 Barbary, K. 2016, *J. Open Source Softw.*, 1, 58
 Barnes, D. G., Staveley-Smith, L., de Blok, W. J. G., et al. 2001, *MNRAS*, 322, 486

Battaglia, G., Tolstoy, E., Helmi, A., et al. 2006, *A&A*, 459, 423
 Battaglia, G., Tolstoy, E., Helmi, A., et al. 2011, *MNRAS*, 411, 1013
 Bellazzini, M., Ibata, R., Monaco, L., et al. 2004, *MNRAS*, 354, 1263
 Belokurov, V., Zucker, D. B., Evans, N. W., et al. 2007, *ApJ*, 654, 897
 Bennet, P., Sand, D. J., Crnojević, D., et al. 2019, *ApJ*, 885, 153
 Bertin, E., & Arnouts, S. 1996, *A&AS*, 117, 393
 Binggeli, B. 1994, *Eur. S. Obs. Conf. Workshop Proc.*, 49, 13
 Binggeli, B., Tarenghi, M., & Sandage, A. 1990, *A&A*, 228, 42
 Bullock, J. S., & Boylan-Kolchin, M. 2017, *ARA&A*, 55, 343
 Buzzoni, A., Arnaboldi, M., & Corradi, R. L. M. 2006, *MNRAS*, 368, 877
 Caldwell, N., Strader, J., Sand, D. J., Willman, B., & Seth, A. C. 2017, *PASA*, 34, e039
 Cappellari, M., & Emsellem, E. 2004, *PASP*, 116, 138
 Chilingarian, I. V., Afanasiev, A. V., Grishin, K. A., Fabricant, D., & Moran, S. 2019, *ApJ*, 884, 79
 Collins, M. L. M., Chapman, S. C., Rich, R. M., et al. 2013, *ApJ*, 768, 172
 Collins, M. L. M., Martin, N. F., Rich, R. M., et al. 2015, *ApJ*, 799, L13
 Correnti, M., Bellazzini, M., & Ferraro, F. R. 2009, *MNRAS*, 397, L26
 Côté, P., McLaughlin, D. E., Hanes, D. A., et al. 2001, *ApJ*, 559, 828
 Crnojević, D., Grebel, E. K., & Koch, A. 2010, *A&A*, 516, A85
 Crnojević, D., Rejkuba, M., Grebel, E. K., Da Costa, G., & Jerjen, H. 2011a, *A&A*, 530, A58
 Crnojević, D., Grebel, E. K., & Cole, A. A. 2011b, *A&A*, 530, A59
 Crnojević, D., Grebel, E. K., & Cole, A. A. 2012, *A&A*, 541, A131
 Crnojević, D., Sand, D. J., Zaritsky, D., et al. 2016a, *ApJ*, 824, L14
 Crnojević, D., Sand, D. J., Spekkens, K., et al. 2016b, *ApJ*, 823, 19
 Crnojević, D., Sand, D. J., Bennet, P., et al. 2019, *ApJ*, 872, 80
 Cusano, F., Garofalo, A., Clementini, G., et al. 2016, *ApJ*, 829, 26
 Da Costa, G. S., Rejkuba, M., Jerjen, H., & Grebel, E. K. 2010, *ApJ*, 708, L121
 Danieli, S., van Dokkum, P., Conroy, C., Abraham, R., & Romanowsky, A. J. 2019, *ApJ*, 874, L12
 Della Bruna, L., Adamo, A., Bik, A., et al. 2020, *A&A*, 635, A134
 Dolphin, A. 2016, *Astrophysics Source Code Library* [record ascl:1608.013]
 Duc, P.-A., Cuillandre, J.-C., Karabal, E., et al. 2015, *MNRAS*, 446, 120
 Eigenthaler, P., Puzia, T. H., Taylor, M. A., et al. 2018, *ApJ*, 855, 142
 Emsellem, E., van der Burg, R. F. J., Fensch, J., et al. 2019, *A&A*, 625, A76
 Evans, C. J., Castro, N., Gonzalez, O. A., et al. 2019, *A&A*, 622, A129
 Fahrion, K., Georgiev, I., Hilker, M., et al. 2019a, *A&A*, 625, A50
 Fahrion, K., Lyubenova, M., van de Ven, G., et al. 2019b, *A&A*, 628, A92
 Fahrion, K., Müller, O., Rejkuba, M., et al. 2020a, *A&A*, 634, A53
 Fahrion, K., Lyubenova, M., Hilker, M., et al. 2020b, *A&A*, 637, A26
 Famaey, B., & McGaugh, S. S. 2012, *Liv. Rev. Relativ.*, 15, 10
 Famaey, B., McGaugh, S., & Milgrom, M. 2018, *MNRAS*, 480, 473
 Fensch, J., van der Burg, R. F. J., Jěřábková, T., et al. 2019, *A&A*, 625, A77
 Ferguson, H. C., & Binggeli, B. 1994, *A&ARv*, 6, 67
 Ferrarese, L., Côté, P., Sánchez-Janssen, R., et al. 2016, *ApJ*, 824, 10
 Forbes, D. A., Alabi, A., Brodie, J. P., et al. 2017, *AJ*, 153, 114
 Forbes, D. A., Alabi, A., Romanowsky, A. J., Brodie, J. P., & Arimoto, N. 2020, *MNRAS*, 492, 4874
 Gannon, J. S., Forbes, D. A., Romanowsky, A. J., et al. 2020, *MNRAS*, 495, 2582
 Geha, M., van der Marel, R. P., Guhathakurta, P., et al. 2010, *ApJ*, 711, 361
 Geha, M., Blanton, M. R., Yan, R., & Tinker, J. L. 2012, *ApJ*, 757, 85
 Geha, M., Wechsler, R. H., Mao, Y.-Y., et al. 2017, *ApJ*, 847, 4
 Georgiev, I. Y., Puzia, T. H., Goudfrooij, P., & Hilker, M. 2010, *MNRAS*, 406, 1967
 Grebel, E. K. 2016, in *Star Clusters and Black Holes in Galaxies Across Cosmic Time*, eds. Y. Meiron, S. Li, F. K. Liu, & R. Spurzem, *IAU Symp.*, 312, 157
 Guérou, A., Krajinović, D., Epinat, B., et al. 2017, *A&A*, 608, A5
 Hagh, H., Kroupa, P., Banik, I., et al. 2019, *MNRAS*, 487, 2441
 Hamraz, E., Peletier, R. F., Khosroshahi, H. G., et al. 2019, *A&A*, 625, A94
 Hanuschik, R., Data Processing, & Quality Control Group 2017, *ESO Calibration Workshop: The Second Generation VLT Instruments and Friends*, 15
 Hargis, J. R., Kimmig, B., Willman, B., et al. 2016, *ApJ*, 818, 39
 Harris, W. E., & van den Bergh, S. 1981, *AJ*, 86, 1627
 Harris, G. L. H., Rejkuba, M., & Harris, W. E. 2010, *PASA*, 27, 457
 Harris, W. E., Harris, G. L. H., & Alessi, M. 2013, *ApJ*, 772, 82
 Henden, A. A., Welch, D. L., Terrell, D., & Levine, S. E. 2009, *Am. Astron. Soc. Meet. Abstr.*, 214, 669
 Hidalgo, S. L., Monelli, M., Aparicio, A., et al. 2013, *ApJ*, 778, 103
 Huang, K.-W., & Koposov, S. E. 2021, *MNRAS*, 500, 986
 Jaffé, Y. L., Aragón-Salamanca, A., Ziegler, B., et al. 2014, *MNRAS*, 440, 3491
 Javanmardi, B., Martínez-Delgado, D., Kroupa, P., et al. 2016, *A&A*, 588, A89
 Jerjen, H., & Rejkuba, M. 2001, *A&A*, 371, 487
 Jerjen, H., Binggeli, B., & Freeman, K. C. 2000, *AJ*, 119, 593
 Karachentsev, I. D., & Kaisin, S. S. 2020, *MNRAS*, 495, 3592
 Karachentsev, I. D., Sharina, M. E., Dolphin, A. E., et al. 2002, *A&A*, 385, 21

- Karachentsev, I. D., Karachentseva, V. E., Huchtmeier, W. K., & Makarov, D. I. 2004, *AJ*, **127**, 2031
- Karachentsev, I. D., Tully, R. B., Dolphin, A., et al. 2007, *AJ*, **133**, 504
- Karachentsev, I. D., Makarov, D. I., & Kaisina, E. I. 2013, *AJ*, **145**, 101
- Kewley, L. J., Nicholls, D. C., & Sutherland, R. S. 2019, *ARA&A*, **57**, 511
- Kim, D., & Jerjen, H. 2015, *ApJ*, **808**, L39
- Kirby, E. N., Lanfranchi, G. A., Simon, J. D., Cohen, J. G., & Guhathakurta, P. 2011, *ApJ*, **727**, 78
- Kirby, E. N., Cohen, J. G., Guhathakurta, P., et al. 2013, *ApJ*, **779**, 102
- Kirshner, R. P., & Taylor, K. 1976, *ApJ*, **208**, L83
- Koch, A., Grebel, E. K., Wyse, R. F. G., et al. 2006, *AJ*, **131**, 895
- Koch, A., Wilkinson, M. I., Kleyna, J. T., et al. 2009, *ApJ*, **690**, 453
- Koposov, S. E., Belokurov, V., Torrealba, G., & Evans, N. W. 2015, *ApJ*, **805**, 130
- Kormendy, J., Fisher, D. B., Cornell, M. E., & Bender, R. 2009, *ApJS*, **182**, 216
- Kroupa, P. 2001, *MNRAS*, **322**, 231
- Kroupa, P., Haghi, H., Javanmardi, B., et al. 2018, *Nature*, **561**, E4
- Laporte, C. F. P., Agnello, A., & Navarro, J. F. 2019, *MNRAS*, **484**, 245
- Lelli, F., Fraternali, F., & Verheijen, M. 2014, *A&A*, **563**, A27
- Lelli, F., McGaugh, S. S., Schombert, J. M., & Pawlowski, M. S. 2017, *ApJ*, **836**, 152
- Levesque, E. M., Kewley, L. J., & Larson, K. L. 2010, *AJ*, **139**, 712
- Lianou, S., Grebel, E. K., & Koch, A. 2010, *A&A*, **521**, A43
- Lim, S., Peng, E. W., Côté, P., et al. 2018, *ApJ*, **862**, 82
- Lisker, T., Grebel, E. K., & Binggeli, B. 2008, *AJ*, **135**, 380
- Lupton, R. 2005, *Transformations Between SDSS Magnitudes and Other Systems*, <https://www.sdss3.org/dr10/algorithms/sdssUBVRTtransform.php/>
- Mackey, A. D., & Gilmore, G. F. 2003a, *MNRAS*, **338**, 120
- Mackey, A. D., & Gilmore, G. F. 2003b, *MNRAS*, **340**, 175
- Makarov, D. I., Sharina, M. E., Karachentseva, V. E., & Karachentsev, I. D. 2015, *A&A*, **581**, A82
- Martel, A. R., Ford, H. C., Bradley, L. D., et al. 2004, *AJ*, **128**, 2758
- Martin, N. F., de Jong, J. T. A., & Rix, H.-W. 2008, *ApJ*, **684**, 1075
- Martin, N. F., McConnachie, A. W., Irwin, M., et al. 2009, *ApJ*, **705**, 758
- Martin, N. F., Chambers, K. C., Collins, M. L. M., et al. 2014, *ApJ*, **793**, L14
- Martin, N. F., Collins, M. L. M., Longeard, N., & Tollerud, E. 2018, *ApJ*, **859**, L5
- Mateo, M. L. 1998, *ARA&A*, **36**, 435
- Mateo, M., Olszewski, E. W., & Walker, M. G. 2008, *ApJ*, **675**, 201
- Mau, S., Cerny, W., Pace, A. B., et al. 2020, *ApJ*, **890**, 136
- McConnachie, A. W. 2012, *AJ*, **144**, 4
- McGaugh, S. S., & de Blok, W. J. G. 1998, *ApJ*, **499**, 41
- McGaugh, S. S., Lelli, F., & Schombert, J. M. 2016, *Phys. Rev. Lett.*, **117**, 201101
- McGaugh, S. S., Schombert, J. M., & Lelli, F. 2017, *ApJ*, **851**, 22
- Milgrom, M. 1983, *ApJ*, **270**, 365
- Misgeld, I., & Hilker, M. 2011, *MNRAS*, **414**, 3699
- Moumen, I., Robert, C., Devost, D., et al. 2019, *MNRAS*, **488**, 803
- Müller, O., Jerjen, H., Pawlowski, M. S., & Binggeli, B. 2016, *A&A*, **595**, A119
- Müller, O., Jerjen, H., & Binggeli, B. 2017, *A&A*, **597**, A7
- Müller, O., Pawlowski, M. S., Jerjen, H., & Lelli, F. 2018a, *Science*, **359**, 534
- Müller, O., Rejkuba, M., & Jerjen, H. 2018b, *A&A*, **615**, A96
- Müller, O., Ibata, R., Rejkuba, M., & Posti, L. 2019a, *A&A*, **629**, L2
- Müller, O., Rejkuba, M., Pawlowski, M. S., et al. 2019b, *A&A*, **629**, A18
- Müller, O., Famaey, B., & Zhao, H. 2019c, *A&A*, **623**, A36
- Müller, O., Marleau, F. R., Duc, P.-A., et al. 2020, *A&A*, **640**, A106
- Muñoz, R. R., Côté, P., Santana, F. A., et al. 2018, *ApJ*, **860**, 66
- Oey, M. S., Meurer, G. R., Yelda, S., et al. 2007, *ApJ*, **661**, 801
- Peng, C. Y., Ho, L. C., Impey, C. D., & Rix, H.-W. 2002, *AJ*, **124**, 266
- Peng, E. W., Jordán, A., Côté, P., et al. 2008, *ApJ*, **681**, 197
- Phillips, M. M., Jenkins, C. R., Dopita, M. A., Sadler, E. M., & Binette, L. 1986, *AJ*, **91**, 1062
- Pietrinferni, A., Cassisi, S., Salaris, M., & Castelli, F. 2004, *ApJ*, **612**, 168
- Pota, V., Forbes, D. A., Romanowsky, A. J., et al. 2013, *MNRAS*, **428**, 389
- Prole, D. J., Hilker, M., van der Burg, R. F. J., et al. 2019, *MNRAS*, **484**, 4865
- Reid, W. A. 2015, *IAU Gen. Assem.*, **29**, 2249670
- Rejkuba, M., Da Costa, G. S., Jerjen, H., Zoccali, M., & Binggeli, B. 2006, *A&A*, **448**, 983
- Rejkuba, M., Harris, W. E., Greggio, L., et al. 2014, *ApJ*, **791**, L2
- Ryś, A., Falcón-Barroso, J., & van de Ven, G. 2013, *MNRAS*, **428**, 2980
- Saifollahi, T., Trujillo, I., Beasley, M. A., Peletier, R. F., & Knapen, J. H. 2021, *MNRAS*, in press [arXiv:2006.14630]
- Sandage, A., & Binggeli, B. 1984, *AJ*, **89**, 919
- Scott, N., Eftekhari, F. S., Peletier, R. F., et al. 2020, *MNRAS*, **497**, 1571
- Simon, J. D., & Geha, M. 2007, *ApJ*, **670**, 313
- Soto, K. T., Lilly, S. J., Bacon, R., Richard, J., & Conseil, S. 2016, *MNRAS*, **458**, 3210
- Stein, Y., Bomans, D. J., Kamphuis, P., et al. 2018, *A&A*, **620**, A29
- Strader, J., Brodie, J. P., Spitler, L., & Beasley, M. A. 2006, *AJ*, **132**, 2333
- Strader, J., Seth, A. C., Forbes, D. A., et al. 2013, *ApJ*, **775**, L6
- Streich, D., de Jong, R. S., Bailin, J., et al. 2014, *A&A*, **563**, A5
- Tafelmeyer, M., Jablonka, P., Hill, V., et al. 2010, *A&A*, **524**, A58
- Taibi, S., Battaglia, G., Kacharov, N., et al. 2018, *A&A*, **618**, A122
- Taibi, S., Battaglia, G., Rejkuba, M., et al. 2020, *A&A*, **635**, A152
- Tammann, G. A. 1994, *Eur. S. Obs. Conf. Workshop Proc.*, **49**, 3
- Taylor, M. A., Muñoz, R. P., Puzia, T. H., et al. 2016, ArXiv e-prints [arxiv:1608.07285]
- Taylor, M. A., Puzia, T. H., Muñoz, R. P., et al. 2017, *MNRAS*, **469**, 3444
- Taylor, M. A., Eigenthaler, P., Puzia, T. H., et al. 2018, *ApJ*, **867**, L15
- Teeninga, P., Moschini, U., Trager, S., & Wilkinson, M. 2013, *Power*, **2**, 1
- Teeninga, P., Moschini, U., Trager, S. C., & Wilkinson, M. H. 2015, *International Symposium on Mathematical Morphology and its Applications to Signal and Image Processing* (Springer), 157
- Tollerud, E. J., Beaton, R. L., Geha, M. C., et al. 2012, *ApJ*, **752**, 45
- Toloba, E., Guhathakurta, P., Boselli, A., et al. 2015, *ApJ*, **799**, 172
- Tolstoy, E., Irwin, M. J., Helmi, A., et al. 2004, *ApJ*, **617**, L119
- Tolstoy, E., Hill, V., & Tosi, M. 2009, *ARA&A*, **47**, 371
- Torrealba, G., Koposov, S. E., Belokurov, V., et al. 2016, *MNRAS*, **463**, 712
- Tully, R. B., Libeskind, N. I., Karachentsev, I. D., et al. 2015, *ApJ*, **802**, L25
- Valdes, F., Gruendl, R., & DES Project 2014, in *Astronomical Data Analysis Software and Systems XXIII*, eds. N. Manset, & P. Forshay, *ASP Conf. Ser.*, **485**, 379
- van Dokkum, P., Danieli, S., Cohen, Y., et al. 2018, *Nature*, **555**, 629
- van Dokkum, P., Danieli, S., Abraham, R., Conroy, C., & Romanowsky, A. J. 2019, *ApJ*, **874**, L5
- Vazdekis, A., Sánchez-Blázquez, P., Falcón-Barroso, J., et al. 2010, *MNRAS*, **404**, 1639
- Vazdekis, A., Koleva, M., Ricciardelli, E., Röck, B., & Falcón-Barroso, J. 2016, *MNRAS*, **463**, 3409
- Venhola, A., Peletier, R., Laurikainen, E., et al. 2019, *A&A*, **625**, A143
- Voggel, K. T., Seth, A. C., Neumayer, N., et al. 2018, *ApJ*, **858**, 20
- Voggel, K. T., Seth, A. C., Sand, D. J., et al. 2020, *ApJ*, **899**, 140
- Walker, M. G., Mateo, M., Olszewski, E. W., et al. 2009, *ApJ*, **704**, 1274
- Walsh, J. R., Rejkuba, M., & Walton, N. A. 2015, *A&A*, **574**, A109
- Weilbacher, P. M., Streicher, O., Urrutia, T., et al. 2012, in *Software and Cyberinfrastructure for Astronomy II*, Proc. SPIE, **8451**, 84510B
- Weilbacher, P. M., Palsa, R., Streicher, O., et al. 2020, *A&A*, **641**, A28
- Weisz, D. R., Dalcanton, J. J., Williams, B. F., et al. 2011, *ApJ*, **739**, 5
- Weisz, D. R., Dolphin, A. E., Skillman, E. D., et al. 2014, *ApJ*, **789**, 147
- Willman, B., Dalcanton, J. J., Martínez-Delgado, D., et al. 2005, *ApJ*, **626**, L85
- Wolf, J., Martínez, G. D., Bullock, J. S., et al. 2010, *MNRAS*, **406**, 1220
- York, D. G., Adelman, J., Anderson, J. E., Jr., et al. 2000, *AJ*, **120**, 1579

Appendix A: Surface brightness photometry of KK 203

Due to the lack of surface brightness photometry of the dwarf galaxy KK 203 in the literature, we have derived it here. We used archival g and r band imaging taken with the Dark Energy Camera. The stacked g band image has an exposure time of 1000 s, the r band an exposure time of 60 s. The data was processed by the standard DECam community pipeline (Valdes et al. 2014). To model the surface brightness profile of the galaxy, we fit Sérsic profiles to the galaxy using GALFIT (Peng et al. 2002). We provided GALFIT with a segmentation map created by MTOObjects (Teeninga et al. 2013, 2015) to mask foreground stars and background galaxies. The zero points were derived using The AAVSO Photometric All-Sky Survey (APASS) standard stars (Henden et al. 2009). We derive an extinction corrected apparent magnitude of $m_g = 16.28$ mag with a color of $(g - r)_0 = 0.22$ mag. The effective radius is 19.8 arcsec, which corresponds to 361 pc at the distance of KK 203 ($D = 3.77$ Mpc). The mean effective surface brightness is $\mu_{\text{eff},g} = 24.75$ mag. Using the color transformation by Lupton (2005), we derive an absolute magnitude of $M_V = -11.7$ mag, which is slightly brighter than what is listed in the literature (Müller et al. 2019b).

Appendix B: Properties of the background objects

Our MUSE data of KK 198 and dw1315–45 revealed that these two galaxies are not dwarf galaxies associated with the Centaurus group but rather are background star forming galaxies. Both KK 198 and dw1315–45 show strong Balmer emission lines ($H\alpha$ and $H\beta$) as well as [NII], [SII], and [OIII] lines. KK 198 has a redshift of 0.0128, dw1315–45 of 0.0100, which puts them at a distance of ≈ 50 Mpc. The former is a face-on spiral galaxy, as already noted in the optical FORS2 images (Müller et al. 2019b), the latter must be an ultra-diffuse galaxy with an effective radius of ≈ 2300 pc.

Appendix C: Spectra of the targets

In Fig. C.1 we present all the integrated spectra of our targets. The best fit provided by pPXF includes the stellar absorption and emission lines. Two targets (KK 198 and dw1315–45) are clearly background star-forming galaxies with strong emission lines.

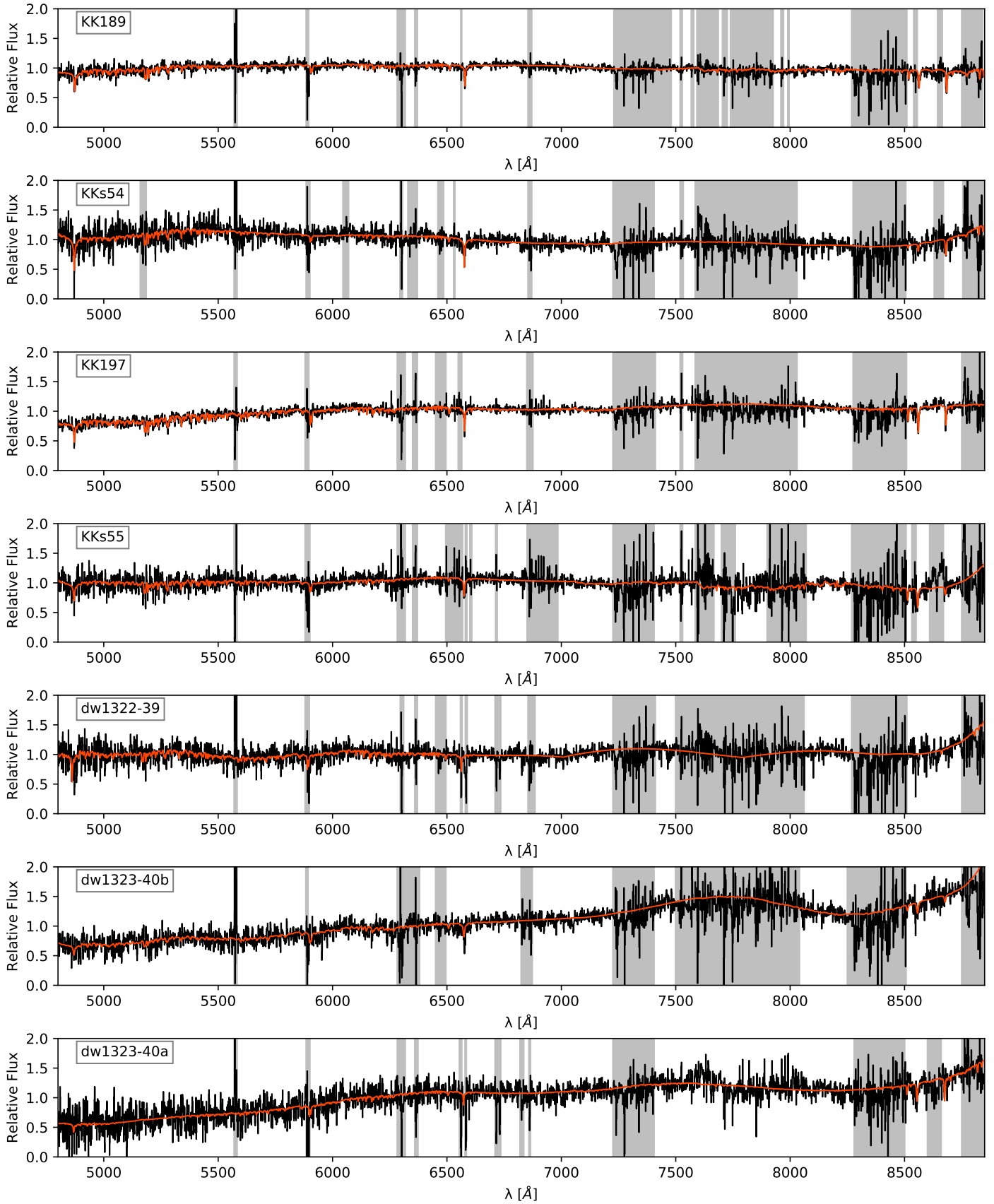


Fig. C.1. Integrated MUSE spectra (black) of all the observed targets. The gray area are masked regions, the red lines correspond to the best-fit from pPXF.

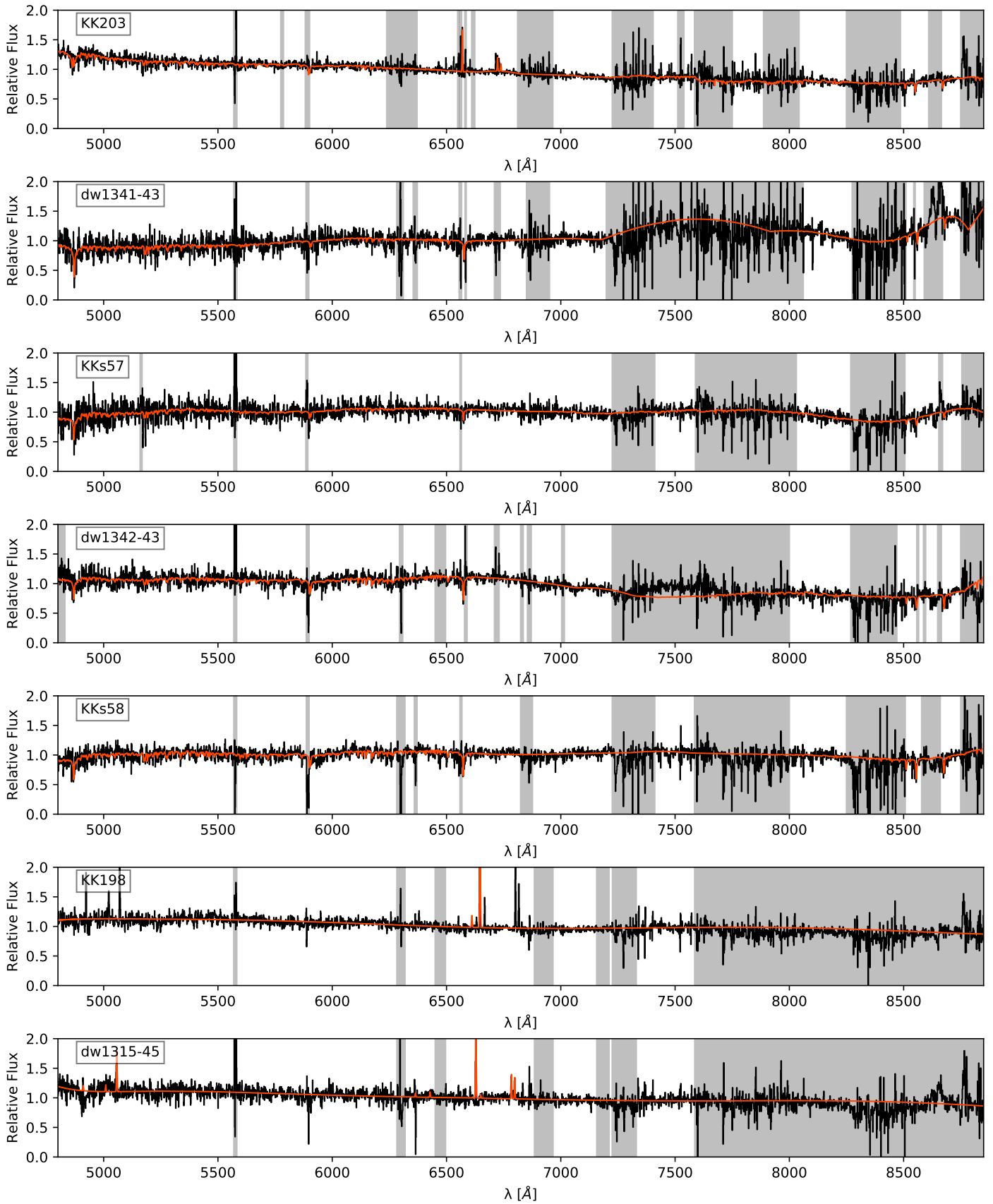


Fig. C.1. continued.